Scaling and universality in the counterion-condensation transition at charged cylinders

Ali Naji* and Roland R. Netz
Physics Department, Technical University of Munich, D-85748 Garching, Germany
(Received 26 October 2005; published 8 May 2006)

Counterions at charged rodlike polymers exhibit a condensation transition at a critical temperature (or, equivalently, at a critical linear charge density for polymers), which dramatically influences various static and dynamic properties of charged polymer solutions. We address the critical and universal aspects of this transition for counterions at a single charged cylinder in two and three spatial dimensions using numerical and analytical methods. By introducing a Monte Carlo sampling method in logarithmic radial scale, we are able to numerically simulate the critical limit of infinite system size (corresponding to the infinite-dilution limit) within tractable equilibration times. The critical exponents are determined for the inverse moments of the counterionic density profile (which play the role of the order parameters and represent the mean inverse localization length of counterions) both within mean-field theory and within Monte Carlo simulations. In three dimensions (3D), we demonstrate that correlation effects (neglected within mean-field theory) lead to an excessive accumulation of counterions near the charged cylinder below the critical temperature (i.e., in the condensation phase), while surprisingly, the critical region exhibits universal critical exponents in accordance with mean-field theory. Also in contrast with the typical trend in bulk critical phenomena, where fluctuations become more enhanced in lower dimensions, we demonstrate, using both numerical and analytical approaches, that mean-field theory becomes exact for the two-dimensional (2D) counterion-cylinder system at all temperatures (Manning parameters), when the number of counterions tends to infinity. For a finite number of particles, however, the 2D problem displays a series of peculiar singular points (with diverging heat capacity), which reflect successive delocalization events of individual counterions from the central cylinder. In both 2D and 3D, the heat capacity shows a universal jump at the critical point and the internal energy develops a pronounced peak. The asymptotic behavior of the energy peak location is used to determine the critical temperature, which is also found to be in agreement with the mean-field prediction.

DOI: 10.1103/PhysRevE.73.056105 PACS number(s): 64.60.Fr, 61.20.Ja, 82.35.Rs, 87.15.−v

I. INTRODUCTION

Electrostatics of charged polymer solutions is often dominated by small oppositely charged ions (counterions) that maintain their global electroneutrality. Many charged polymers, such as tubulin, actin, *fd*-viruses, and DNA, are stiff and may be represented by straight cylinders (on length scales smaller than the persistence length). Neglecting many-ion effects, a single counterion is attracted by an electrostatic potential that grows logarithmically with the radial distance from the central cylinder. But since the counterion confinement entropy also shows a logarithmic dependence on the radial distance, it was suggested by Onsager [1] that a counterion delocalization transition occurs at a critical cylinder charge or, equivalently, at a critical temperature. Onsager's argument, which is strictly valid for a single particle, was soon corroborated by mean-field studies [1–14], which demonstrate that a charged cylinder can indeed bind or condense a finite fraction of counterions below a critical temperature (even in the limit of infinite system size with no confining boundaries), while above the critical temperature, all counterions decondense and diffuse to infinity.

This *counterion-condensation transition* (CCT) dramatically affects a whole number of static and dynamic quantities as observed in recent experiments on charged polymers [1,2,6,7,15–21]: upon condensation, the polymer charge is screened, leading, for instance, to a significant reduction in electrophoretic mobility [18,21] and conductivity [20] of polymers. It also triggers striking phenomena such as counterion-induced attraction between like-charged polymers, which is believed to be responsible for the formation of compact phases of F-actin [22] and DNA [23]. Since its discovery, counterion condensation has been at the focus of numerical [24–28] and analytical [28–50] studies.

The CCT at a charged cylinder is regulated by a dimensionless control parameter $\xi=q\ell_B\tau$, known as the Manning parameter [1], which depends on the linear charge density of the cylinder, $-\tau e$, charge valency of counterions, $+q$, and the Bjerrum length $\ell_B=e^2/(4\pi\varepsilon\varepsilon_0 k_B T)$ accommodating the ambient temperature T and the medium dielectric constant ε. The Manning parameter plays the role of the *inverse rescaled temperature* and can be varied experimentally by changing the linear charge density (using synthetic chains or various *p*H) [17,19–21] or by varying the medium dielectric constant (by mixing different solvents) [18,21]. According to mean-field theory [1–14], condensation occurs above the critical value $\xi_c=1$. In experiments, the critical Manning parameter appears to be about unity, but large deviations have also been reported [20,21,51] and the precise location of the critical point is still debated [21].

*Corresponding author. Present address: Department of Physics, and Department of Chemistry and Biochemistry, University of California, Santa Barbara, CA 93106, USA. Electronic address: anaji@chem.ucsb.edu

On the other hand, it is known that the critical temperature may in general be influenced by correlations and fluctuations, which are not captured within mean-field theory [52]. These effects typically cause deviations from mean-field predictions in both nonuniversal and universal quantities below the upper critical dimension. Surprisingly, the mean-field prediction for the CCT threshold, ξ_c, has not been questioned in the literature and apparently assumed to be exact. Likewise, the existence of universal scaling relations and critical exponents associated with the CCT has not been addressed, neither on the mean-field level nor in the presence of correlations.

Our chief goal in this paper is to address the following issues: (i) what is the exact threshold of the CCT, ξ_c, and (ii) what are the critical exponents associated with this transition in three (3D) and two (2D) spatial dimensions. We shall also address the type of singularities that emerge in thermodynamic quantities when the CCT occurs.

To establish a systematic analysis of the correlation effects, we employ Monte Carlo simulations for counterions at a single charged cylinder using a sampling method (centrifugal sampling), which is realized by mapping the radial coordinate to a logarithmic scale. This enables us to investigate the critical behavior of counterions in the limit of infinite system size (i.e., when the lateral confining boundaries tend to infinity) within tractable equilibration times in the simulations. The importance of taking a very large system size becomes evident by noting that the lateral finite-size effects, which mask the critical behavior near ξ_c, depend on the *logarithm* of the system size in the cylindrical geometry [1,2,4,9–13,53–57] and thus cause a quite weak convergence to the critical limit. This will be made clear more systematically later in this paper.

Our simulations provide the first numerical results for the asymptotic properties of the CCT and systematically incorporate correlation effects (a brief report of some of our results has been presented previously in Ref. [28]). Note that the relevance of electrostatic correlations is in general identified by a dimensionless coupling parameter $\Xi=2\pi q^3\ell_B^2\sigma_s$, where $\sigma_s=\tau/(2\pi R)$ is the surface charge density and R the radius of the charged cylinder. Mean-field theory becomes exact in the limit $\Xi\to 0$ [59,60], while in the converse limit of strong coupling, $\Xi\gg 1$, counterionic correlations typically play an important role and lead to drastic changes [58–63].

In order to investigate scaling properties of the CCT in various regimes of the coupling parameter, we focus on the inverse moments of the counterionic density profile, which play the role of the "order parameters" for this transition; they represent the mean inverse localization length of counterions. Using a combined finite-size-scaling analysis with respect to both the lateral size of the system and the number of counterions, we show that the order parameters indeed adopt a scale-invariant form in the vicinity of the critical point. The critical exponents associated with the reduced temperature and the size parameters are determined both within the simulations and also analytically within two limiting theories of the mean field and strong coupling. As a main result, we find that the critical exponents of the CCT are *universal* (that is, independent of the coupling parameter varied over several decades $0.1<\Xi<10^5$) and appear to be in close agreement with the mean-field prediction. Surprisingly, we find that the critical Manning parameter is also universal; it is determined as $\xi_c=1.000\pm 0.002$, which agrees with the mean-field prediction. (This latter quantity is determined from the asymptotic behavior of the location of a singular peak that emerges in the internal energy of the system.) The excess heat capacity is found to vanish at small Manning parameters (i.e., in the decondensation phase) but exhibits a *universal jump* at the transition point, indicating that the CCT may be regarded as a second-order transition as also suggested in a recent mean-field study [40].

As will be shown, the validity of mean-field predictions breaks down in 3D when the Manning parameter is increased beyond the critical value (i.e., in the condensation phase). Here interparticle correlations become significant at large coupling and lead to an enhanced accumulation of counterions near the cylinder surface that agrees with the strong-coupling theory [59–63]. The fraction of condensed counterions (i.e., those counterions that remain associated with the central cylinder in the infinite-system-size limit) is, however, found to be unaffected by the correlations effects. It equals the Manning limiting value at all realistic couplings.

In order to bring out possible role of fluctuations, we also study the CCT in a 2D counterion-cylinder system (equivalent to a 3D system composed of a central charged cylinder and parallel cylindrical "counterions" with logarithmic Coulomb interactions, as may be applicable to an experimental system of oriented cationic and anionic polymers [64–67]). For a finite number of counterions, a peculiar series of singular points emerges in the order parameters and thermodynamic quantities that reflect successive delocalization events of individual counterions as the Manning parameter varies. As the number of particles increases, the singular points tend to merge, and eventually in the thermodynamic limit, the 2D results tend to the mean-field predictions. Therefore, in contrast to the typical situation in bulk critical phenomena, the CCT in 2D is found to be in *exact* agreement with mean-field theory for the whole range of Manning parameters (rescaled temperatures) when the number of counterions tends to infinity. As will be shown, the simulation results in 2D can be reproduced using an approximate analytical approach. A more systematic theory for the 2D problem has been developed recently in Ref. [46].

The organization of this paper is as follows: in Secs. II–VI, we focus on the counterion-cylinder system in three dimensions. Our model is introduced in Sec. II, where we shall also outline the general method proposed for the investigation of the CCT. In Sec. III, we derive the scaling relations for order parameters and determine the asymptotic behavior of thermodynamic quantities within mean-field theory (which is the same in all dimensions). In Sec. IV, analytical results are obtained within the strong-coupling theory. The numerical analysis of the CCT for various coupling strengths will be presented in Secs. V–VIII in three and two dimensions.

II. COUNTERION-CONDENSATION TRANSITION IN THREE DIMENSIONS

A. Cell model for charged rodlike polymers

We consider a standard, primitive cell model [53–57], consisting of a single charged cylinder of radius R and point-

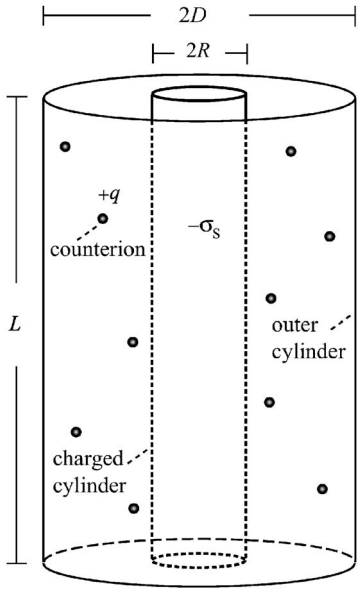

FIG. 1. The three-dimensional model consists of a charged cylinder of infinite length L and its neutralizing counterions confined in a cylindrical box (see the text for parameters).

like neutralizing counterions of charge valency $+q$ that are confined laterally in an outer (coaxial) cylindrical box of radius D—see Fig. 1. The cylinder has an infinite length L and a uniform (surface) charge distribution $-\sigma(\mathbf{x})e$, where $\sigma(\mathbf{x})=\sigma_s\delta(r-R)$. (Note that q and σ_s are given in units of the elementary charge e and are positive by definition.) The cylinder is assumed to be rigid and impenetrable to counterions and the dielectric medium is represented by a uniform dielectric constant ε. In three dimensions, electric charges interact via bare Coulombic interaction

$$v_{3D}(\mathbf{x})=\frac{1}{|\mathbf{x}|}. \tag{1}$$

The electroneutrality condition holds globally inside the cell and entails the relation

$$qN=\tau L, \tag{2}$$

where N is the number of counterions in the cell and $\tau=2\pi R\sigma_s$ represents the linear charge density of the cylinder. The system is described by the Hamiltonian

$$\frac{\mathcal{H}_N}{k_BT}=q^2\ell_B\sum_{\langle ij\rangle}v_{3D}(\mathbf{x}_i-\mathbf{x}_j)-q\ell_B\sum_{i=1}^{N}\int v_{3D}(\mathbf{x}-\mathbf{x}_i)\sigma(\mathbf{x})d\mathbf{x}+\frac{\ell_B}{2}\int\sigma(\mathbf{x})v_{3D}(\mathbf{x}-\mathbf{x}')\sigma(\mathbf{x}')d\mathbf{x}\,d\mathbf{x}', \tag{3}$$

which comprises Coulomb repulsion between counterions located at $\{\mathbf{x}_i\}$ (first term), counterion-cylinder attraction (second term), and the self-energy of the cylinder (last term). It can be written as

$$\frac{\mathcal{H}_N}{k_BT}=q^2\ell_B\sum_{\langle ij\rangle}v_{3D}(\mathbf{x}_i-\mathbf{x}_j)+2\xi\sum_{i=1}^{N}\ln\left(\frac{r_i}{R}\right)+C_0, \tag{4}$$

where $r_i=(x_i^2+y_i^2)^{1/2}$ is the radial distance of the ith counterion from the cylinder axis (z axis) and ξ is the *Manning parameter* of the system [1],

$$\xi=q\ell_B\tau, \tag{5}$$

with $\ell_B=e^2/(4\pi\varepsilon\varepsilon_0k_BT)$ being the Bjerrum length (in water and at room temperature $\ell_B\simeq 7$ Å). The additive term C_0 in Eq. (4) is related to the cylinder self-energy; it will be important in obtaining a convergent energy expression in the simulations (Sec. V B and Appendix D).

B. Dimensionless description

The parameter space of the system may be spanned by a minimal set of independent dimensionless parameters given by the ratios between characteristic length scales. These length scales are the rescaled Bjerrum length $q^2\ell_B$, the Gouy-Chapman length

$$\mu=\frac{1}{2\pi q\ell_B\sigma_s}, \tag{6}$$

and the radius of the charged cylinder, R, and that of the outer boundary, D. The rescaled cylinder radius

$$\tilde{R}=\frac{R}{\mu}=\xi \tag{7}$$

equals the Manning parameter ξ. The ratio between the rescaled Bjerrum length and the Gouy-Chapman length gives the so-called *electrostatic coupling parameter* [59],

$$\Xi=\frac{q^2\ell_B}{\mu}=2\pi q^3\ell_B^2\sigma_s, \tag{8}$$

which, in general, identifies the importance of electrostatic correlations in a charged system [59–63]. The ratio between the length scales D and R enters only through its logarithm [53,54]

$$\Delta\equiv\ln\left(\frac{D}{R}\right), \tag{9}$$

which will be referred to hereafter as the *lateral extension parameter*.

The dimensionless form of the Hamiltonian is obtained by rescaling the spatial coordinates as $\tilde{\mathbf{x}}=\mathbf{x}/\mu$ [59]—i.e.,

$$\frac{\mathcal{H}_N}{k_BT}=\Xi\sum_{\langle ij\rangle}v_{3D}(\tilde{\mathbf{x}}_i-\tilde{\mathbf{x}}_j)+2\xi\sum_{i=1}^{N}\ln\left(\frac{\tilde{r}_i}{\tilde{R}}\right)+C_0. \tag{10}$$

The electroneutrality condition (2) in rescaled units reads

$$2\pi\xi\tilde{L}=2\pi\Xi N, \tag{11}$$

with the left-hand side being simply the rescaled area of the cylinder covered by electric charges. The thermodynamic limit is obtained for $N\to\infty$ and $L\to\infty$, but keeping $N/L=\tau/q$ (or, equivalently, $N/\tilde{L}=\xi/\Xi$) fixed.

C. CCT as a generic binding-unbinding transition

The statistical physics of the present model may be investigated using the canonical partition function

$$\mathcal{Z}_N = \frac{\mu^{3N}}{N!}\int_{\widetilde{V}}\left[\prod_{i=1}^{N} d\widetilde{z}_i\, d\phi_i\, d\widetilde{r}_i\, \widetilde{r}_i\right]\exp\left\{-\frac{\mathcal{H}_N}{k_BT}\right\}, \quad (12)$$

represented in cylindrical coordinates $\widetilde{\mathbf{x}}_i=(\widetilde{r}_i,\phi_i,\widetilde{z}_i)$, with the spatial integral running over the volume $\widetilde{V}$ of the space accessible for counterions—i.e., $\widetilde{R}\leqslant\widetilde{r}\leqslant\widetilde{D}$.

Naively, one may conjecture that the partition function (12) diverges in a certain range of Manning parameters, when the upper boundary of the radial integrals, $\widetilde{D}$, tends to infinity [68], because the logarithmic form of the counterion-cylinder interaction gives rise to algebraic prefactors of the form $\widetilde{r}_i^{1-2\xi}$ in the integrand. The possible emergence of a divergency in a charged cylindrical system was first pointed out by Onsager and the connection with the counterion-condensation transition was discussed by Manning [1].

Here we demonstrate this peculiar point using a transformation of coordinates, which provides the basis for our numerical simulations considered later in Secs. V and VI. The radial coordinate is transformed as

$$y = \ln\left(\frac{\widetilde{r}}{\widetilde{R}}\right), \quad (13)$$

upon which the partition function in Eq. (12) transforms as

$$\mathcal{Z}_N = \frac{\mu^{3N}\widetilde{R}^{2N}}{N!}\int_{\widetilde{V}}\left[\prod_{i=1}^{N} d\widetilde{z}_i\, d\phi_i\, dy_i\right]\exp\left\{-\frac{\mathcal{H}^*_N}{k_BT}\right\}, \quad (14)$$

where the volume integral runs over the region $0\leqslant y\leqslant\Delta=\ln(D/R)$ and

$$\frac{\mathcal{H}^*_N}{k_BT} = \sum_{i=1}^{N} W(y_i) + \Xi\sum_{\langle ij\rangle} v_{3D}(\widetilde{\mathbf{x}}_i-\widetilde{\mathbf{x}}_j) + C_0 \quad (15)$$

is the transformed Hamiltonian of the system with

$$W(y) = 2(\xi-1)y. \quad (16)$$

As seen, the original partition function is now mapped to the partition function of a system of interacting (repelling) particles in a *linear* potential well $W(y)$. This latter quantity includes the counterion-cylinder attraction potential $2\xi y$, as well as a fictitious *centrifugal* potential $-2y$, from the measure of the radial integral.

For small Manning parameter $\xi<1$, the potential well $W(y)$ becomes purely repulsive suggesting that counterions *unbind* (or "decondense") from the central cylinder departing to infinity as the outer boundary tends to infinity, $\Delta=\ln(D/R)\to\infty$, while for $\xi>1$, the potential well exerts an attractive force upon counterions. This might lead to *partial binding* (or "condensation") of counterions even in the absence of confining walls. The new representation of $\mathcal{Z}_N$, Eq. (14), therefore, reflects the interplay between energetic and entropic factors on a microscopic level.

Note that the rigorous analytical derivation of the aforementioned unbinding transition (based on the full partition function) is still missing and only limiting cases have been examined analytically (Sec. II E).

D. Onsager instability

As a simple illustrative case, let us consider a "hypothetical" system, in which mutual counterionic repulsions are switched off. The partition function (12) thus factorizes as $\mathcal{Z}_N\sim\mathcal{Z}_1^N$, where

$$\mathcal{Z}_1 = \int_0^{\Delta} dy\, e^{2(1-\xi)y} = \frac{e^{2(1-\xi)\Delta}-1}{2(1-\xi)} \quad (17)$$

is the single-particle partition function. It diverges for $\xi<1$, when the lateral extension parameter tends to infinity, $\Delta\to\infty$, which implies complete counterion decondensation, because the probability $P(r)\sim\exp(-2\xi\ln r)/\mathcal{Z}_1$ of finding counterions at any finite distance r from the cylinder tends to zero [equivalent to a vanishing density profile, $\rho(r)=NP(r)$]. But $\mathcal{Z}_1$ and thus the counterionic density profile remain finite for $\xi>1$, indicating that $\xi_c=1$ is the onset of the CCT on the *single-particle* level, which we shall term here as the *Onsager instability* (in the spirit of Onsager's original argument [1]). Onsager instability captures the basic features of the CCT. It exhibits the characteristic logarithmic convergence (via $\Delta=\ln D/R$) to the critical limit as the volume per polymer ($\sim D^2$) goes to infinity. Also as we show in Appendix A, it displays algebraic singularities in energy and heat capacity at $\xi_c=1$, which may be characterized by a set of scaling exponents. Such scaling properties play a crucial in our analysis of the CCT in the following sections.

We emphasize here that the results obtained within Onsager instability are by no means conclusive since, as will be shown later, interparticle interactions lead to qualitative differences. In particular, it turns out that a diverging partition function is *not* necessarily an indication of the *onset* of the CCT as asserted by the forgoing single-particle argument.

E. Beyond the Onsager instability: Many-body effects and electrostatic correlations

Many-body contributions involved in the full partition function (12) render systematic analysis of the CCT quite difficult. The analytical results are available in the asymptotic limits of (i) vanishing coupling parameter $\Xi\to 0$, which leads to mean-field or Poisson-Boltzmann (PB) theory, and (ii) infinite coupling parameter $\Xi\to\infty$, which leads to the strong-coupling (SC) theory [59]. In the mean-field approximation [case (i)], statistical correlations among counterions are systematically neglected. In the opposite limit of strong coupling [case (ii)], the leading contribution to the partition function takes a very simple form comprising only the one-particle (counterion-cylinder) contributions; it results from strong electrostatic correlations between counterions near the surface [59–63,69]. We study the mean-field predictions for the CCT in Sec. III. The SC description resembles the Onsager instability and will be discussed in Sec. IV. The perturbative improvement of these two limiting theories for *finite* coupling parameter is formally possible by computing higher-order correction terms (as previously per-

formed for planar charged walls [59,60,62,63]), but will not be considered here.

Interestingly, in both limiting cases, the CCT threshold is found to be the same—i.e., $\xi_c=1$—which is due to the simplified form of the counterionic correlations. An important question is whether the critical Manning parameter ξ_c varies with the coupling parameter in the intermediate regime. Such a behavior may be expected because the Manning parameter represents the rescaled inverse temperature of the system [i.e., $\xi=T_*/T$ with $T_*\equiv q\tau e^2/(4\pi\varepsilon\varepsilon_0 k_B)$], which, as known from bulk critical phenomena [52], may be shifted from its mean-field value due to interparticle correlations. Also it is interesting to examine whether the CCT exhibits scale-invariant properties near ξ_c and if it can be classified in terms of a universal class of critical scaling exponents. In general, critical scaling relations represent the relevant characteristic properties of continuous phase transitions [52].

To address these issues, one has to define quantities which can serve as *order parameters* of the CCT. In the following section, we shall introduce such quantities and, by focusing on the mean-field limit, show that the order parameters indeed exhibit scaling behavior near the critical point. We return to the influence of electrostatic correlations on the critical Manning parameter and scaling exponents of the CCT in the subsequent sections.

III. MEAN-FIELD THEORY FOR THE COUNTERION-CONDENSATION TRANSITION

A. Nonlinear Poisson-Boltzmann equation

The mean-field theory can be derived systematically using a saddle-point analysis in the limit $\Xi\to 0$ [59]. It is governed by the well-known Poisson-Boltzmann equation, which, in rescaled units, reads (Appendix B)

$$\nabla_{\tilde{\mathbf{x}}}^2\psi_{\mathrm{PB}}=2\tilde{\sigma}(\tilde{\mathbf{x}})-\tilde{\kappa}^2\tilde{\Omega}(\tilde{\mathbf{x}})e^{-\psi_{\mathrm{PB}}(\tilde{\mathbf{x}})} \tag{18}$$

for the dimensionless potential field $\psi_{\mathrm{PB}}(\tilde{\mathbf{x}})$. Here

$$\tilde{\sigma}(\tilde{\mathbf{x}})=\delta(\tilde{r}-\tilde{R}) \tag{19}$$

is the rescaled charge distribution of the cylinder and

$$\tilde{\Omega}(\tilde{\mathbf{x}})=\tilde{\Omega}(\tilde{r})=\begin{cases}1, & \tilde{R}\leqslant\tilde{r}\leqslant\tilde{D},\\ 0, & \text{otherwise},\end{cases} \tag{20}$$

specifies the volume accessible to counterions. In the canonical ensemble, one has

$$\frac{\tilde{\kappa}^2}{2}=\frac{2\pi\xi\tilde{L}}{\int d\tilde{\mathbf{x}}\,\tilde{\Omega}(\tilde{\mathbf{x}})\exp(-\psi_{\mathrm{PB}})}. \tag{21}$$

Assuming the cylindrical symmetry (for an infinite cylinder) and using Eq. (18) together with the global electroneutrality condition (11), one obtains

$$\left(\tilde{r}\frac{d\psi_{\mathrm{PB}}}{d\tilde{r}}\right)_{\tilde{r}=\tilde{R}}=2\xi,\quad \left(\tilde{r}\frac{d\psi_{\mathrm{PB}}}{d\tilde{r}}\right)_{\tilde{r}=\tilde{D}}=0, \tag{22}$$

which are used to solve the PB equation (18) in the nontrivial region $\tilde{R}\leqslant\tilde{r}\leqslant\tilde{D}$ [53,54]. Thereby, one obtains both the free energy (Sec. III D) and the rescaled radial density profile of counterions:

$$\tilde{\rho}_{\mathrm{PB}}(\tilde{r})=\frac{\tilde{\kappa}^2}{2}\tilde{\Omega}(\tilde{r})e^{-\psi_{\mathrm{PB}}(\tilde{r})}. \tag{23}$$

The rescaled density profile $\tilde{\rho}_{\mathrm{PB}}(\tilde{r})$ is related to the actual *number* density of counterions, $\rho_{\mathrm{PB}}(r)$, through $\tilde{\rho}_{\mathrm{PB}}(\tilde{r})=\rho_{\mathrm{PB}}(r)/(2\pi\ell_{\mathrm{B}}\sigma_s^2)$ [59] (Appendix B).

As shown by Fuoss *et al.* [54], the PB solution takes different functional forms depending on whether ξ lies below or above the threshold:

$$\Lambda_*=\frac{\Delta}{1+\Delta}, \tag{24}$$

that is,

$$\psi_{\mathrm{PB}}(\tilde{r})=\begin{cases}\ln\left[\dfrac{\tilde{\kappa}^2\tilde{r}^2}{2\beta^2}\sinh^2\left(\beta\ln\dfrac{\tilde{r}}{\tilde{R}}+\coth^{-1}\dfrac{\xi-1}{\beta}\right)\right], & \xi\leqslant\Lambda_*,\\ \ln\left[\dfrac{\tilde{\kappa}^2\tilde{r}^2}{2\beta^2}\sin^2\left(\beta\ln\dfrac{\tilde{r}}{\tilde{R}}+\cot^{-1}\dfrac{\xi-1}{\beta}\right)\right], & \xi\geqslant\Lambda_*,\end{cases} \tag{25}$$

where β is given by the transcendental equations

$$\xi=\begin{cases}\dfrac{1-\beta^2}{1-\beta\coth(-\beta\Delta)}, & \xi\leqslant\Lambda_*,\\ \dfrac{1+\beta^2}{1-\beta\cot(-\beta\Delta)}, & \xi\geqslant\Lambda_*.\end{cases} \tag{26}$$

The PB density profile of counterions, Eq. (23), is then obtained for $\tilde{R}\leqslant\tilde{r}\leqslant\tilde{D}$ as

$$\tilde{\rho}_{\mathrm{PB}}(\tilde{r})=\frac{\beta^2}{\tilde{r}^2}\times\begin{cases}\sinh^{-2}\left(\beta\ln\dfrac{\tilde{r}}{\tilde{R}}+\coth^{-1}\dfrac{\xi-1}{\beta}\right), & \xi\leqslant\Lambda_*,\\ \sin^{-2}\left(\beta\ln\dfrac{\tilde{r}}{\tilde{R}}+\cot^{-1}\dfrac{\xi-1}{\beta}\right), & \xi\geqslant\Lambda_*,\end{cases} \tag{27}$$

where we have arbitrarily chosen $\psi_{\mathrm{PB}}(\tilde{r}=\tilde{R})=0$ to fix the reference of the potential. This condition also fixes $\tilde{\kappa}$ in Eq. (25) as well as the radial density of counterions *at contact* with the cylinder using Eq. (23)—i.e.,

$$\frac{\tilde{\kappa}^2}{2}=\tilde{\rho}_{\mathrm{PB}}(\tilde{R})=\frac{1}{\xi^2}\times\begin{cases}(\xi-1)^2-\beta^2, & \xi\leqslant\Lambda_*,\\ (\xi-1)^2+\beta^2, & \xi\geqslant\Lambda_*.\end{cases} \tag{28}$$

The density profiles given by Eq. (27) are normalized to the total number of counterions, N, a condition imposed via Eq.

(21). Using Eq. (23), the normalization condition in rescaled units reads (Appendix B)

$$\int_{\tilde{R}}^{\tilde{D}} d\tilde{r}\,\tilde{r}\,\tilde{\rho}_{\mathrm{PB}}(\tilde{r}) = \xi. \tag{29}$$

B. Threshold of the CCT within PB theory

The threshold of the counterion-condensation transition within the PB theory, ξ_c^{PB}, was investigated by several workers [9–14,54]. It can be determined from the asymptotic ($\Delta \to \infty$) behavior of the density profile as briefly reviewed below.

First note that for $\Delta \gg 1$, the threshold Λ_*, Eq. (24), tends to unity from below, i.e.

$$\Lambda_* = 1 - \frac{1}{\Delta} + O(\Delta^{-2}). \tag{30}$$

Therefore, for Manning parameter $\xi < 1$, one may use the first relation in Eq. (26) to obtain the limiting behavior of the integration constant β as (Appendix C 1)

$$\beta = (1 - \xi) + O(e^{-2\Delta(1-\xi)}), \tag{31}$$

when $\Delta \to \infty$. Using this in Eq. (28), one finds that the density of counterions at contact, $\tilde{\rho}_{\mathrm{PB}}(\tilde{R})$, asymptotically vanishes. Hence, the density profile (23) at any finite distance from the cylinder tends to zero,

$$\tilde{\rho}_{\mathrm{PB}}(\tilde{r}) \to 0, \tag{32}$$

for $\xi \leqslant 1$ and in the limit $\Delta \to \infty$, which represents the decondensation regime. For $\xi > 1$, on the other hand, one has $\beta \to 0$ as Δ increases to infinity (Appendix C 1), and thus using Eq. (28), one obtains

$$\tilde{\rho}_{\mathrm{PB}}(\tilde{R}) \to \frac{(\xi - 1)^2}{\xi^2}. \tag{33}$$

Using the second relation in Eq. (27) and expanding for small β, the radial density profile follows as [10,70]

$$\tilde{\rho}_{\mathrm{PB}}(\tilde{r}) \to \frac{(\xi - 1)^2}{\xi^2}\left[\frac{\tilde{r}}{\tilde{R}}\right]^{-2}\left[1 + (\xi - 1)\ln\frac{\tilde{r}}{\tilde{R}}\right]^{-2} \tag{34}$$

in the limit $\Delta \to \infty$, which is finite and therefore indicates condensation of counterions (see also Appendix C 4). This proves that the mean-field critical point is given by

$$\xi_c^{\mathrm{PB}} = 1, \tag{35}$$

corresponding to the mean-field critical temperature

$$T_c^{\mathrm{PB}} = \frac{q\tau e^2}{4\pi\varepsilon\varepsilon_0 k_B}. \tag{36}$$

C. Critical scale invariance: Mean-field exponents

It is readily seen from Eqs. (33) and (34) that the asymptotic density of counterions adopts a scale-invariant or homogeneous form with respect to the *reduced Manning parameter*,

$$\zeta = 1 - \frac{\xi_c^{\mathrm{PB}}}{\xi}, \tag{37}$$

in the vicinity of the critical point. Note that the reduced Manning parameter equals the *reduced temperature* of the system, $t = 1 - (T/T_c^{\mathrm{PB}})$, when other quantities such as the dielectric constant ε and the linear charge density of the cylinder, τ, are fixed. (Experimentally, however, the Manning parameter is varied by changing ε [18,21] or τ [17,19–21] at constant temperature, in which case, ζ can be related to the reduced dielectric constant or the reduced linear charge density.)

In a finite confining box (finite Δ), such scaling forms with respect to ζ do not hold because the true CCT is suppressed (i.e., the counterion density does not strictly vanish at $\xi_c^{\mathrm{PB}} = 1$). Yet as a general trend [52], we expect that for *sufficiently large* Δ, the reminiscence of such scaling relations appears in the form of finite-size-scaling relations near the transition point. These relations would involve both ζ and the lateral extension parameter Δ (as the only relevant parameters in the mean-field limit) in a scale-invariant fashion as will be shown below.

As possible candidates for the CCT "order parameters," we use the inverse moments of the counterionic density profile:

$$S_n \equiv \left\langle \frac{1}{\tilde{r}^n} \right\rangle = \frac{\int_{\tilde{R}}^{\tilde{D}} \tilde{r}\,d\tilde{r}\,\tilde{r}^{-n}\tilde{\rho}(\tilde{r})}{\int_{\tilde{R}}^{\tilde{D}} \tilde{r}\,d\tilde{r}\,\tilde{\rho}(\tilde{r})}, \tag{38}$$

where $n > 0$ [71]. Note that these quantities reflect *mean inverse localization length* of counterions. In the condensation phase (where counterions adopt a finite density profile), one has $S_n > 0$, indicating a finite localization length. But at the critical point and in the decondensation phase (with vanishing counterion density), one has $S_n = 0$ in the limit of infinite system size $\Delta \to \infty$, indicating a diverging counterion localization length.

In order to derive the mean-field finite-size-scaling relations for S_n, we focus on the PB solution in the regime of Manning parameters $\xi \geqslant \Lambda_*$, since for any finite Δ, we have $\Lambda_* \leqslant \xi_c^{\mathrm{PB}} = 1$ from Eq. (24). Inserting the first relation of Eq. (27) into Eq. (38), we obtain

$$S_n^{\mathrm{PB}} = \frac{\beta^2}{\xi}\int_{\tilde{R}}^{\tilde{D}} d\tilde{r}\,\tilde{r}^{-n-1}\sin^{-2}\left(\beta\ln\frac{\tilde{r}}{\tilde{R}} + \cot^{-1}\frac{\xi - 1}{\beta}\right). \tag{39}$$

Changing the integration variable as $y = \ln(\tilde{r}/\tilde{R})$, we get

$$S_n^{\mathrm{PB}} = \frac{\beta^2}{\xi^{n+1}}\int_0^{\Delta} dy\,e^{-ny}\sin^{-2}\left(\beta y + \cot^{-1}\frac{\xi - 1}{\beta}\right). \tag{40}$$

For $\Delta \gg 1$, the above relation may be approximated by a simple analytic expression as (Appendix C 3)

$$S_n^{\mathrm{PB}}(\zeta,\Delta) \simeq \frac{1}{n}\left[\zeta^2 + \beta^2(\zeta,\Delta)\right] \tag{41}$$

for $\zeta = 1 - \xi_c^{\mathrm{PB}}/\xi$ being sufficiently close to the critical value $\zeta_c^{\mathrm{PB}} = 0$.

Using the above result, we may distinguish two limiting cases, where different scaling relations emerge: (i) when $\Delta \to \infty$ but ζ is *finite* and close to the critical value and (ii) when Δ is finite and large, but ζ tends toward the critical value—i.e., $\zeta \to \zeta_c^{\mathrm{PB}} = 0$.

In the limiting case (i), as stated before, we have $\beta \to 0$ for the above-threshold regime, $\zeta \geqslant 0$; thus, using Eq. (41), we obtain

$$S_n^{\mathrm{PB}}(\zeta, \Delta \to \infty) \simeq \frac{\zeta^2}{n}. \tag{42}$$

On the other hand, S_n^{PB} vanishes for $\zeta \leqslant 0$ (Appendix C 3). Hence, the following scaling relation is obtained in the infinite-system-size limit $\Delta \to \infty$:

$$S_n^{\mathrm{PB}}(\zeta, \infty) \simeq \begin{cases} \zeta^{\chi_{\mathrm{PB}}}/n, & 0 \leqslant \zeta \ll 1, \\ 0, & \zeta \leqslant 0, \end{cases} \tag{43}$$

which introduces the mean-field critical exponent associated with the reduced Manning parameter, ζ (or the reduced temperature t) as

$$\chi_{\mathrm{PB}} = 2. \tag{44}$$

The mean-field counterion-condensation transition is therefore characterized by a diverging (localization) length scale $1/S_1^{\mathrm{PB}} \sim \zeta^{-2}$ as the critical point is approached from above. The scaling relation (43) may also be derived in a direct way by considering an unbounded system ($\Delta = \infty$) as shown in Appendix C 4.

In the limiting case (ii) with $\zeta \to \zeta_c^{\mathrm{PB}} = 0$, we have from Eq. (26) that $\beta \simeq \pi/(2\Delta)$ when Δ is finite but large, $\Delta \gg 1$ (Appendix C 1). Therefore, Eq. (41) gives

$$S_n^{\mathrm{PB}}(0,\Delta) \simeq \frac{\pi^2}{4n\Delta^2}, \tag{45}$$

which introduces a new scaling relation

$$S_n^{\mathrm{PB}}(0,\Delta) \sim \Delta^{-\gamma_{\mathrm{PB}}} \tag{46}$$

with the mean-field critical exponent

$$\gamma_{\mathrm{PB}} = 2 \tag{47}$$

associated with the lateral extension parameter Δ. This finite-size relation shows that the approach to the true critical limit (where S_n^{PB} vanishes at the critical point) is *logarithmically* weak as the box size D increases to infinity—i.e., $S_n^{\mathrm{PB}}(\zeta = 0) \sim 1/(\ln D/R)^2$.

The scaling relations (43) and (45) indicate that S_n^{PB} takes a scale-invariant form with respect to ζ and Δ as

$$S_n^{\mathrm{PB}}(\zeta,\Delta) \simeq \Delta^{-\gamma_{\mathrm{PB}}} \mathcal{D}_n(\zeta \Delta^{\gamma_{\mathrm{PB}}/\chi_{\mathrm{PB}}}) \tag{48}$$

for sufficiently large Δ and in the vicinity of the critical point. The scaling function $\mathcal{D}_n(u)$ has the following asymptotic behavior:

$$\mathcal{D}_n(u) \sim \begin{cases} (\text{const}), & u \to 0, \\ u^{\chi_{\mathrm{PB}}}/n, & u \to +\infty. \end{cases} \tag{49}$$

Formally, such scale-invariant relations within the PB theory are closely connected with the fact that the integration constant $\beta(\zeta,\Delta)$ takes a scale-invariant form

$$\beta \simeq \Delta^{-1} \mathcal{B}(\zeta\Delta) \tag{50}$$

near the critical point. Here $\mathcal{B}(u)$ is a scaling function which behaves asymptotically as (Appendix C 1)

$$\mathcal{B}(u) \sim \begin{cases} \text{const}, & u \to 0, \\ \sqrt{u}, & u \to +\infty. \end{cases} \tag{51}$$

Combining Eqs. (41) and (50), the scaling function $\mathcal{D}_n(u)$ is obtained in terms of $\mathcal{B}(u)$ as

$$\mathcal{D}_n(u) \simeq \frac{1}{n}[u^2 + \mathcal{B}^2(u)], \tag{52}$$

which reproduces Eq. (49) when combined with Eq. (51).

Note that the mean-field critical exponents χ_{PB} and γ_{PB} are independent of the density moment index n. These exponents may be used to characterize the mean-field universality class in *all* dimensions, since the PB results are independent of the space dimension [72].

D. Mean-field energy and heat capacity

As shown in a previous work [73], the mean-field canonical free energy of the counterion-cylinder system may be obtained using a saddle-point analysis from the field-theoretic representation of the partition function in the limit $\Xi \to 0$ [59]. The rescaled PB free energy $\tilde{\mathcal{F}}^{\mathrm{PB}} \equiv \mathcal{F}_N^{\mathrm{PB}}/(Nk_BT)$ is given (discarding the trivial kinetic energy part) by

$$\tilde{\mathcal{F}}^{\mathrm{PB}} = -\frac{1}{\xi}\int \tilde{r}\, d\tilde{r}\left[\frac{1}{4}\left(\frac{d\psi_{\mathrm{PB}}}{d\tilde{r}}\right)^2 + \delta(\tilde{r}-\tilde{R})\psi_{\mathrm{PB}}(\tilde{r})\right] - \ln\left[\frac{1}{\xi}\int_{\tilde{R}}^{\tilde{D}} \tilde{r}\, d\tilde{r}\, e^{-\psi_{\mathrm{PB}}(\tilde{r})}\right] - \ln\left(\frac{2V_{\mathrm{cyl}}}{N\xi}\right), \tag{53}$$

where $V_{\mathrm{cyl}} = \pi R^2 L$ is the actual volume of the cylinder. In the thermodynamic limit $N \to \infty$, the ratio V_{cyl}/N is a constant and will be dropped in what follows.

Inserting the PB potential field, Eq. (25), into the free energy expression (53), we find that, for $\xi \geqslant \Lambda_*$,

$$\tilde{\mathcal{F}}^{\mathrm{PB}} = -\frac{1}{\xi}\left[(1-\beta^2)\Delta + \ln\left(\frac{(\xi-1)^2+\beta^2}{1+\beta^2}\right) + \xi\right] + \ln[(\xi-1)^2+\beta^2] - \ln(2\xi), \tag{54}$$

while for $\xi \leqslant \Lambda_*$, we have

$$\tilde{\mathcal{F}}^{\mathrm{PB}} = -\frac{1}{\xi}\left[(1+\beta^2)\Delta + \ln\left(\frac{(\xi-1)^2-\beta^2}{1-\beta^2}\right) + \xi\right] + \ln[(\xi-1)^2-\beta^2] - \ln(2\xi). \tag{55}$$

These expressions (up to some additive constants) have also

been obtained by Lifson and Katchalsky [55] using a charging-process method.

The rescaled (excess) internal energy $\tilde{E}^{\mathrm{PB}} \equiv E_N^{\mathrm{PB}}/(Nk_BT)$ and the rescaled (excess) heat capacity $\tilde{C}^{\mathrm{PB}} \equiv C_N^{\mathrm{PB}}/(Nk_B)$ can be calculated using the thermodynamic relations

$$\tilde{E}^{\mathrm{PB}} = \xi \frac{\partial \tilde{\mathcal{F}}^{\mathrm{PB}}}{\partial \xi}, \tag{56}$$

$$\tilde{C}^{\mathrm{PB}} = -\xi^2 \frac{\partial^2 \tilde{\mathcal{F}}^{\mathrm{PB}}}{\partial \xi^2}, \tag{57}$$

where the derivatives are taken at fixed volume, number of particles, and also fixed charges and dielectric constant. A closed-form expression may be obtained for the internal energy using the relation $E_N^{\mathrm{PB}} = (\varepsilon\varepsilon_0/2)\int d\mathbf{x}(\nabla\varphi_{\mathrm{PB}})^2$, where $\varphi_{\mathrm{PB}} = k_BT\psi_{\mathrm{PB}}/qe$ is the potential field in actual units. In rescaled units, the result is

$$\tilde{E}^{\mathrm{PB}} = \frac{1}{4\xi}\int_{\tilde{R}}^{\tilde{D}} \tilde{r}\, d\tilde{r}\left(\frac{d\psi_{\mathrm{PB}}}{d\tilde{r}}\right)^2 \tag{58}$$

$$= \frac{1}{\xi} \times \begin{cases} (1+\beta^2)\Delta + \ln\left[\dfrac{(\xi-1)^2-\beta^2}{1-\beta^2}\right] + \xi, & \xi \leqslant \Lambda_*, \\ (1-\beta^2)\Delta + \ln\left[\dfrac{(\xi-1)^2+\beta^2}{1+\beta^2}\right] + \xi, & \xi \geqslant \Lambda_*. \end{cases} \tag{59}$$

In general, the thermodynamic quantities can be calculated numerically using the transcendental equation (26) for β. But in the limit $\Delta \to \infty$, the asymptotic form of β (Appendix C 1) may be used to obtain the asymptotic rescaled PB free energy [73]

$$\tilde{\mathcal{F}}^{\mathrm{PB}} = \begin{cases} (\xi-2)\Delta, & \xi \leqslant \xi_c^{\mathrm{PB}} = 1, \\ -\Delta/\xi, & \xi \geqslant \xi_c^{\mathrm{PB}} = 1. \end{cases} \tag{60}$$

The asymptotic rescaled PB energy follows as

$$\tilde{E}^{\mathrm{PB}} = \begin{cases} \xi\Delta, & \xi \leqslant \xi_c^{\mathrm{PB}}, \\ \Delta/\xi, & \xi \geqslant \xi_c^{\mathrm{PB}}, \end{cases} \tag{61}$$

and the rescaled PB heat capacity as

$$\tilde{C}^{\mathrm{PB}} = \begin{cases} 0, & \xi < \xi_c^{\mathrm{PB}}, \\ 2\Delta/\xi, & \xi > \xi_c^{\mathrm{PB}}. \end{cases} \tag{62}$$

The above results show that both the internal energy and the heat capacity develop a singular peak at the critical Manning parameter $\xi_c^{\mathrm{PB}} = 1$ when the limit $\Delta \to \infty$ is approached. The PB results also show that the free energy diverges with Δ *both* above and below the critical point, indicating that, in contrast to the behavior obtained within the single-particle Onsager instability [1] (Sec. II D and Appendix A), a diverging partition function is not in general an indication of the onset of the CCT.

Another important point is that the PB heat capacity exhibits a discontinuity at $\xi_c^{\mathrm{PB}} = 1$. Therefore, the CCT may be regarded as a second-order transition as also pointed out in a previous mean-field study [40]. We shall return to the singular behavior of energy and heat capacity later in our numerical studies.

IV. STRONG-COUPLING THEORY

In the limit of infinite coupling parameter, $\Xi \to \infty$, the partition function of a charged system adopts an expansion in powers of $1/\Xi$, the leading term of which comprises only single-particle contributions [59,60]. This leading-order theory, referred to as the asymptotic strong-coupling theory, describes the complementary limit to mean-field theory, where interparticle correlations are expected to become important [59–63].

The rescaled SC density profile for counterions is obtained as

$$\tilde{\rho}_{\mathrm{SC}}(\tilde{r}) = \lambda_0 \tilde{\Omega}(\tilde{r}) e^{-\tilde{u}(\tilde{r})}, \tag{63}$$

where $\tilde{u}(\tilde{r}) = 2\xi \ln(\tilde{r}/\tilde{R})$ is the single-particle interaction energy and λ_0 is a normalization factor which is fixed by the total number of counterions; it reads

$$\lambda_0 = \frac{2(\xi-1)}{\xi}\left[1 - e^{-2(\xi-1)\Delta}\right]^{-1}. \tag{64}$$

Note that for $\Delta \to \infty$, λ_0, and therefore the whole density profile, vanishes for $\xi \leqslant 1$. But for $\xi > 1$, one obtains $\lambda_0 \to 2(\xi-1)/\xi$ and hence a finite limiting density profile

$$\tilde{\rho}_{\mathrm{SC}}(\tilde{r}) \to \frac{2(\xi-1)}{\xi}\left(\frac{\tilde{r}}{\tilde{R}}\right)^{-2\xi}. \tag{65}$$

This shows that the CCT is reproduced within the SC theory as well, and surprisingly, the critical Manning parameter is found to be $\xi_c^{\mathrm{SC}} = 1$ in coincidence with the mean-field prediction. Note, however, that the SC profile for $\xi > 1$ indicates a *larger* contact density for counterions as compared with the mean-field result; e.g., for $\Delta \to \infty$, one has

$$\tilde{\rho}_{\mathrm{SC}}(\tilde{R}) = \frac{2(\xi-1)}{\xi}, \tag{66}$$

which is larger than the PB contact value (33) by a factor of $\tilde{\rho}_{\mathrm{SC}}(\tilde{R})/\tilde{\rho}_{\mathrm{PB}}(\tilde{R}) = 2(1-1/\xi)^{-1}$. The SC profile, Eq. (65), also decays faster than the PB profile, Eq. (34), indicating a more compact counterionic layer near the cylinder. This reflects strong ionic correlations in the condensation phase ($\xi > 1$) for $\Xi \gg 1$ as will be discussed further in the numerical studies below.

Using Eq. (63), the SC order parameters can be calculated as

$$S_n^{\mathrm{SC}} = \frac{2(\xi-1)}{\xi^n(2\xi-2+n)}\frac{1-e^{-(2\xi-2+n)\Delta}}{1-e^{-2(\xi-1)\Delta}} \tag{67}$$

for arbitrary ξ and Δ. For $\Delta \to \infty$, S_n^{SC} vanishes for $\xi \leqslant \xi_c^{\mathrm{SC}} = 1$, but takes a limiting form—i.e.,

$$S_n^{\mathrm{SC}} \to \frac{2(\xi-1)}{\xi^n(2\xi-2+n)}, \tag{68}$$

for $\xi \geqslant \xi_c^{\mathrm{SC}}=1$. In the vicinity of the critical point, we find the scaling relation

$$S_n^{\mathrm{SC}}(\zeta,\Delta\to\infty) \simeq \frac{2\zeta}{n}, \tag{69}$$

with the reduced Manning parameter $0<\zeta=1-\xi_c^{\mathrm{SC}}/\xi \ll 1$, which yields the SC critical exponent $\chi_{\mathrm{SC}}=1$. In a finite system and right at the critical point, we find the finite-size-scaling relation

$$S_n^{\mathrm{SC}}(0,\Delta) \simeq \frac{1}{n\Delta}, \tag{70}$$

with the lateral extension parameter $\Delta \gg 1$, which yields the SC critical exponent $\gamma_{\mathrm{SC}}=1$.

These exponents are different from the corresponding mean-field exponents, Eqs. (44) and (47). As will be shown later, the SC theory in general breaks down *near* the CCT critical point, while it remains valid as an asymptotic ($\Xi \to \infty$) theory above the critical point.

V. MONTE CARLO STUDY IN 3D

The preceding analysis reveals a set of scaling relations for the counterion-condensation transition within the mean-field ($\Xi \to 0$) and strong-coupling ($\Xi \to \infty$) theories in the limit of infinite system size. In the following sections, we shall use numerical methods to explore various regimes of the coupling parameter Ξ and, thereby, examine the validity of the aforementioned analytical results.

A. Centrifugal sampling method

A major difficulty in studying the CCT numerically goes back to the lack of an efficient sampling technique. Poor sampling problem arises for counterions at charged curved surfaces in the infinite-volume limit because, contrary to charged plates, a finite fraction of counterions always tends to unbind from curved boundaries and diffuse to infinity as the system relaxes toward its equilibrium state. This situation is, of course, not tractable in simulations; hence, to achieve proper equilibration within a reasonable time, charged cylinders are customarily considered in a confining box (in lateral directions) of *practically* large size. As is well known [4,10–12,25,27], lateral finite-size effects are quite small for sufficiently large Manning parameters ($\xi > \xi_c$). But at small Manning parameters ($\xi \sim \xi_c$), these effects become significant and suppress the decondensation of counterions.

The mean-field results already reveal a very weak convergence to the critical infinite-volume limit for $\xi \sim \xi_c$, which is controlled by the logarithmic size of the confining box $\Delta=\ln(D/R)$. Hence one needs to consider a confining box of extremely large radius D to establish the large-Δ regime, where the scaling (and possibly universal) properties of the CCT emerge. For this purpose, clearly, the simple-sampling methods within Monte Carlo or molecular dynamics schemes [24–27,74–76] are not useful at *low* Manning parameter as they render an infinite relaxation time.

Here we introduce a sampling method within the Monte Carlo scheme, which enables one to properly span the relevant parts of the phase space for large confinement volumes. In three dimensions, we use the configurational Hamiltonian (10) in rescaled coordinates. The sampling method, which we refer to as the *centrifugal sampling*, is obtained by mapping the radial coordinate $\tilde{r}$ to a logarithmic scale according to Eq. (13)—i.e., $y=\ln(\tilde{r}/\tilde{R})$. This leads to the transformed partition function (14). As explained before (Sec. II C), the entropic (centrifugal) factor $\exp(2y)$ is absorbed from the measure of the radial integral into the Hamiltonian, yielding the transformed Hamiltonian $\mathcal{H}_N^*$ in Eq. (15).

We thus simulate the system using Metropolis algorithm [77], but make use of the transformed Hamiltonian (15). The entropic factors, which cause unbinding of counterions, are hence incorporated into the transition probabilities of the associated Markov chain of states that leads to equilibrium states with the distribution function $\sim\exp(-\mathcal{H}_N^*/k_BT)$. The averaged quantities—say, $\bar{Q}$—follow by extracting a set of n_s values $\{Q_1,\ldots,Q_{n_s}\}$ in the course of the simulation as $\bar{Q}=\Sigma_{t=1}^{n_s} Q_t/n_s$, which, for sufficiently large n_s, produces the desired ensemble average $\langle Q\rangle$—i.e.,

$$\bar{Q}=\frac{1}{n_s}\sum_{t=1}^{n_s} Q_t \simeq \frac{\mu^{3N}\tilde{R}^{2N}}{N!\,\mathcal{Z}_N}\int_{\tilde{V}}\left[\prod_{i=1}^{N} d\tilde{z}_i\, d\phi_i\, dy_i\right] \times Q(\{y_i,\phi_i,\tilde{z}_i\})e^{-\mathcal{H}_N^*/k_BT}=\langle Q\rangle, \tag{71}$$

up to relative corrections of the order $1/\sqrt{n_s}$.

B. Simulation model and parameters

The geometry of the counterion-cylinder system in our simulations is similar to what we have sketched in Fig. 1. We use typically between $N=25$ and 300 counterions (most of the results are obtained with $N=100$ and 200) and increase the lateral extension parameter up to $\Delta=300$. We also vary the Manning parameter ξ and consider a wide range of values for the coupling parameter, Ξ, from $\Xi=0.1$ (close to the mean-field regime) up to $\Xi=10^5$ (close to the strong-coupling regime).

The cylindrical simulation box has a finite height $\tilde{L}$, which is set by the electroneutrality condition (11)—i.e., $\tilde{L}=N\Xi/\xi$. In order to mimic the thermodynamic limit and reduce the finite-size effects due to the finiteness of the cylinder height, we apply periodic boundary conditions in the z direction (parallel to the cylinder axis) by replicating the main simulation box infinitely many times in that direction. The long-range character of the Coulomb interaction in such a periodic system leads to the summation of infinite series over all periodic images. These series are not generally convergent, but in an electroneutral system, the divergencies cancel and the series can be converted to fast-converging series. We use the summation techniques due to Lekner [78] and Sperb [79], which are utilized for the one-dimensionally

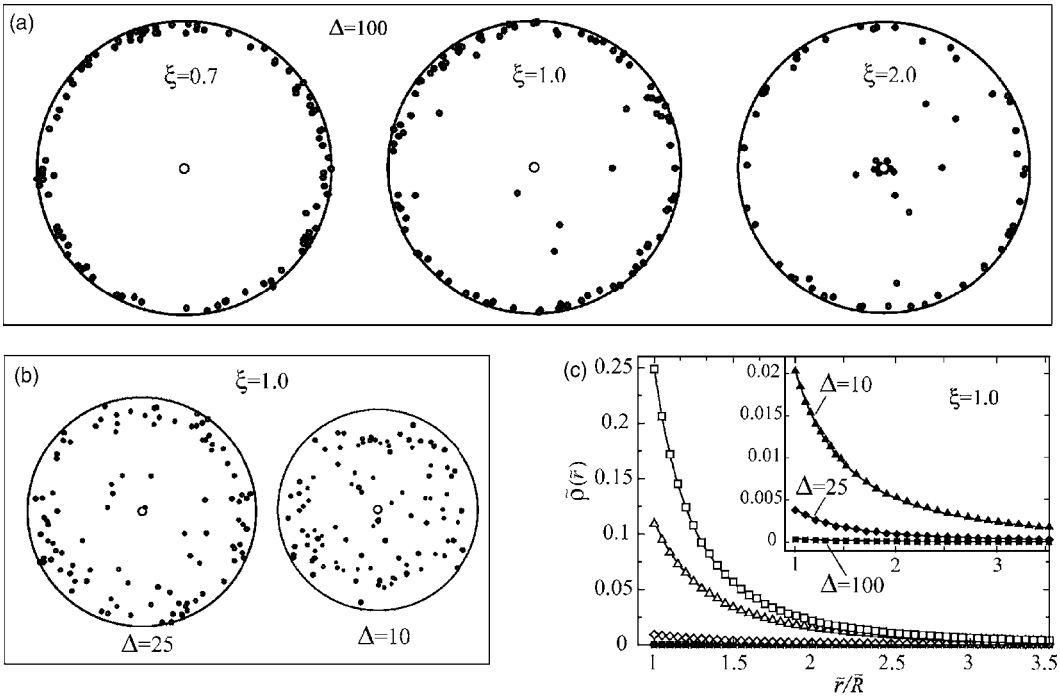

FIG. 2. Typical snapshots from the simulations on the counterion-cylinder system in 3D for (a) lateral extension parameter $\Delta=\ln(D/R)=100$ and three different Manning parameters $\xi=0.7, 1.0$, and 2.0 as indicated on the graph and (b) for Manning parameter $\xi=1.0$ and smaller lateral extension parameters $\Delta=10$ and 25. The snapshots show top views of the simulation box (see Sec. V B and Fig. 1) with radial distances shown in logarithmic scale $y=\ln(\tilde{r}/\tilde{R})$. Pointlike counterions are shown by black spheres and the charged cylinder by a circle in the middle. (c) gives the simulated radial density of counterions in rescaled units, $\tilde{\rho}(\tilde{r})=\rho(r)/(2\pi\ell_B\sigma_s^2)$, as a function of the (linear) distance from the cylinder axis. Main set shows the data for $\Delta=100$ and Manning parameters $\xi=2.0$ (open squares), 1.5 (open up triangles), 1.1 (open diamonds), 1.0 (solid squares), and 0.7 (solid circles) from top to bottom. The inset shows the same for $\xi=1.0$, but for various lateral extension parameters $\Delta=10$, 25, and 100 (top to bottom). Solid curves represent the mean-field PB prediction, Eq. (27). Number of counterions here is $N=100$ and the coupling parameter $\Xi=0.1$. Error bars are smaller than the size of symbols.

periodic system considered here—see Appendix D (similar methods have been developed in Ref. [80]). Finally, in order to obtain reliable values for the error bars, the standard block-averaging scheme is used [81]. The simulations typically run for $\sim 1.1\times 10^6$ Monte Carlo steps per particle with $\sim 10^5$ steps used for the equilibration purpose.

VI. SIMULATION RESULTS IN 3D

A. Global behavior in the infinite-system-size limit

1. Distribution of counterions

Let us start with the distribution of counterions as generated by the centrifugal sampling method. In Fig. 2 typical simulation snapshots are shown together with the counterionic density profile for small coupling parameter $\Xi=0.1$. The counterion distribution is shown for large ($\Delta=100$), intermediate ($\Delta=25$), and small ($\Delta=10$) lateral extension parameters. The counterion-condensation transition is clearly reproduced for large Δ [Fig. 2(a)]: counterions are "decondensed" and gather at the outer boundary at small Manning parameter (shown for $\xi=0.7$), while they partially "condense" and accumulate near the cylinder surface for large Manning parameter (shown for $\xi=2$). The Manning parameter $\xi=1$, as seen, represents an intermediate situation. This trend is demonstrated on a quantitative level by the radial density profile of counterions $\tilde{\rho}(\tilde{r})$ [Fig. 2(c), main set]: $\tilde{\rho}(\tilde{r})$ tends to zero by decreasing ξ down to about unity. Note that relatively large fluctuations occur at low ξ, making $\tilde{\rho}(\tilde{r})$ an inconvenient quantity to precisely locate the critical Manning parameter ξ_c, which will be determined later. The data, moreover, follow the mean-field PB density profile, Eq. (27), shown by solid curves, as expected since the chosen coupling parameter is small.

The transition regime at intermediate ξ exhibits strong finite-size effects. As may be seen from the snapshots in Fig. 2(b), counterion decondensation at $\xi=1$ is strongly suppressed for small logarithmic sizes $\Delta=\ln(D/R)=10$ and 25. Accordingly, the density profiles [inset of Fig. 2(c)] indicate a sizable accumulation of counterions near the cylinder surface, which is in fact washed away by increasing Δ to infinity. Such finite-size effects at low ξ are also observed in previous numerical studies, which have devised simulations in linear scale and thus considered only small confinement volumes per polymer (typically with $\Delta<10$) [25,27,74–76]. In some studies [82], these effects have been interpreted as evidence for counterion condensation at *small* ξ, leading to the incorrect conclusion that no critical transition exists.

2. Condensed fraction of counterions

Our results for large ξ exhibit a counterionic density profile that extends continuously from the cylinder surface to

larger distances. This indicates that making a distinction between two layers of condensed and decondensed counterions, in the sense of two-fluid models frequently used in the literature [1–8,31,33–37,42,43], requires a criterion.

The two-fluid description predicts a fraction

$$\alpha_{\mathrm{M}} = \begin{cases} 0, & \xi \leqslant 1, \\ 1 - 1/\xi, & \xi \geqslant 1, \end{cases} \tag{72}$$

of counterions to reside in the condensed layer (which is considered as a layer with small thickness at the polymer surface), when the infinite-dilution limit is reached. Previous studies [9–11,13,14,25,38,45,47] show that the Manning condensed fraction α_{M} may also be identified systematically within the Poisson-Boltzmann theory. This can be done by employing an *inflection-point criterion* [25,38] for the PB cumulative density, $n_{\mathrm{PB}}(r)$ (the number of counterions inside a cylindrical shell of radius r), which is obtained as

$$\frac{n_{\mathrm{PB}}(r)}{N} = \frac{2\pi L}{N} \int_R^r r'\, dr'\, \rho_{\mathrm{PB}}(r') = \frac{1}{\xi} \times \begin{cases} (\xi - 1) - \beta \coth\left[\beta y + \coth^{-1}\dfrac{\xi - 1}{\beta}\right], & \xi \leqslant \Lambda_*, \\ (\xi - 1) - \beta \cot\left[\beta y + \cot^{-1}\dfrac{\xi - 1}{\beta}\right], & \xi \geqslant \Lambda_*, \end{cases} \tag{73}$$

using Eq. (27). For $\xi \geqslant \Lambda_*$, $n_{\mathrm{PB}}(r)$ exhibits an inflection point at a radial distance r_* when plotted as a function of $y = \ln(r/R)$ [25,38]. One can show that for $\Delta \to \infty$, only the fraction of counterions that lie within the cylindrical region $r \leqslant r_*$ remains associated with the charged cylinder and tends to the Manning condensed fraction—i.e.,

$$\frac{n_{\mathrm{PB}}(r_*)}{N} \to \alpha_{\mathrm{M}}. \tag{74}$$

In other words, only this fraction of counterions contributes to the asymptotic density profile and the rest ($1/\xi$ of all) is pushed to infinity (Appendix C 4).

The simulation results for the cumulative density as a function of the logarithmic radial distance $y = \ln(\tilde{r}/\tilde{R})$ are shown in Fig. 3 for various Manning parameters (solid and dot-dashed curves). Here we have chosen a very large lateral extension parameter $\Delta = \ln(D/R) = 300$, which can exhibit the concept of condensed fraction more clearly. The data show an inflection point located approximately at $y_* = \ln(r_*/R) \simeq \Delta/2$ for large ξ (for $\xi \to 1$, the location of the inflection point, r_*, tends to R; see Appendix C 2). The rapid increase of $n(\tilde{r})$ at small ($r \sim R$) and large distances ($r \sim D$) reflects the two counterion-populated regions at the inner and outer boundaries separated by an extended plateau [compare with Fig. 2(a)]. (A somewhat similar behavior has also been found in an extended two-fluid model [37].) For small Δ, the inflection point has a nonvanishing slope and the two regions are not quite separated (data not shown) [25,38,42,53].

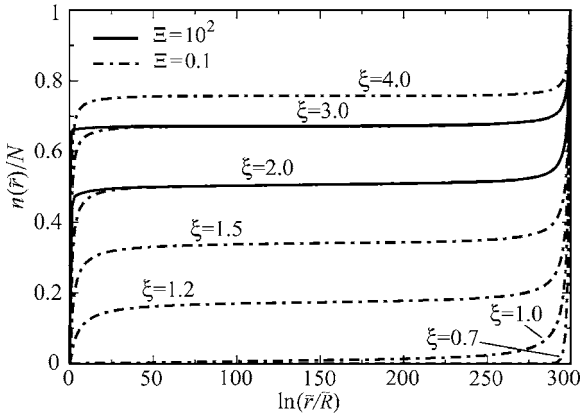

FIG. 3. Cumulative density $n(\tilde{r})$ per total number N of counterions as a function of the logarithmic distance from the charged cylinder, $\ln(\tilde{r}/\tilde{R})$. Dot-dashed curves are the simulation results for $\Xi = 0.1$, $N = 70$, and $\Delta = 300$ and various Manning parameters as shown on the graph. These curves also closely represent the PB prediction (73), which is not explicitly shown. Solid curves show the simulation results for large coupling parameter $\Xi = 10^2$ and for $\xi = 3.0$ and $\xi = 2.0$.

Using the inflection-point criterion, the condensed fraction α may be estimated as $\alpha = n(r_*)/N$, roughly corresponding to the plateau level in Fig. 3. Simulation results for α are shown in Fig. 4 for $\Delta = 300$ (symbols). Let us first consider the case of small coupling parameter $\Xi = 0.1$, where the simulated cumulative density $n(\tilde{r})$ (dot-dashed curves in Fig. 3) closely follows the PB prediction (73) (PB curves are not explicitly shown). In this case, the condensed fraction data (diamonds) agree already quite well (within $<1\%$) with the Manning or PB limiting value α_{M} (solid curve in Fig. 4).

An important question is whether the form of the cumulative density profile $n(\tilde{r})$ and also the condensed fraction are influenced by electrostatic correlations as the coupling parameter increases. In Fig. 3, we show $n(\tilde{r})$ from the simula-

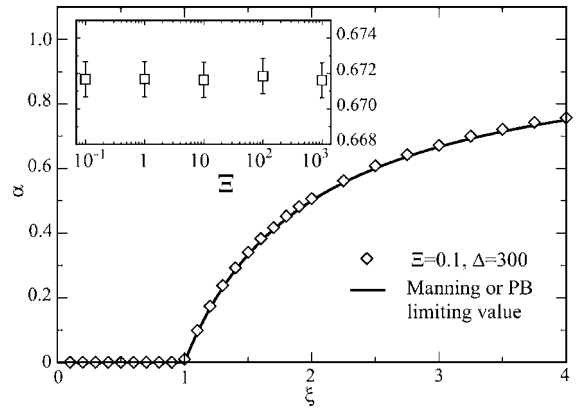

FIG. 4. Main set: simulated condensed fraction of counterions, α, as defined via the inflection-point criterion, as a function of the Manning parameter ξ for $\Xi = 0.1$ (diamonds). Solid curve displays the Manning or PB limiting value α_{M}, for $\Delta = \ln(D/R) \to \infty$ [Eq. (72)]. Inset: condensed fraction as a function of the coupling parameter Ξ for $\xi = 3.0$. These data are obtained for $\Delta = 300$ and $N = 70$.

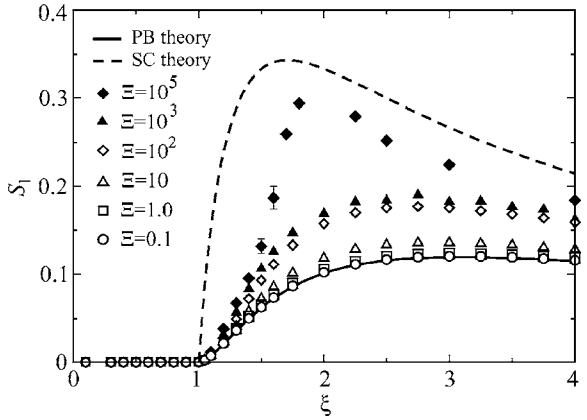

FIG. 5. Simulation data for the order parameter $S_1=\langle 1/\tilde{r}\rangle$ as a function of the Manning parameter ξ for coupling parameters $\Xi=0.1$ up to 10^5 as indicated on the graph. The mean-field (solid line) and the strong-coupling (dashed line) curves are calculated from Eqs. (40) and (67), respectively. The lateral extension parameter is $\Delta=300$, and the number of counterions is $N=200$ for $\Xi=0.1$, $N=50$ for $\Xi=10^5$, and $N=70$ for other coupling parameters.

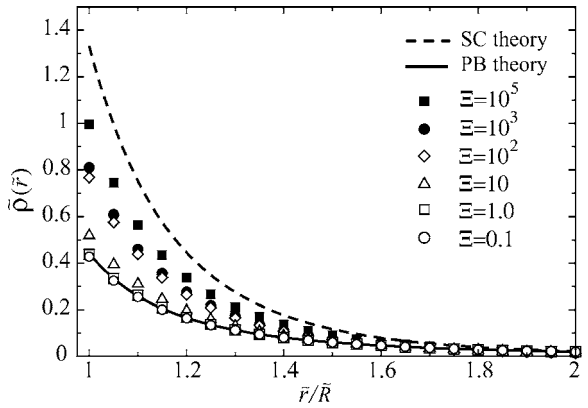

FIG. 6. Rescaled radial density of counterions, $\tilde{\rho}(\tilde{r})=\rho(r)/(2\pi\ell_B\sigma_s^2)$, as a function of the (linear) distance from the cylinder axis for Manning parameter $\xi=3.0$ and various coupling parameters ($\Xi=0.1$ up to 10^5) as shown on the graph. Here $\Delta=300$ and the number of counterions is $N=50$ for $\Xi=10^5$ and $N=70$ for other values of Ξ. The mean-field (solid line) and the strong-coupling (dashed line) curves are obtained from Eqs. (27) and (63), which, for $\Delta=300$, roughly coincide with the asymptotic expressions (34) and (65).

tions for $\Xi=10^2$ and two values of the Manning parameter $\xi=2.0$ and 3.0 (solid curves). This coupling strength generally falls within the strong-coupling regime for charged systems, where electrostatic correlations are expected to play a significant role [62,63] (note that DNA with trivalent counterions represents $\Xi\simeq 75$, but with a larger $\xi\simeq 12$). As seen, $n(\tilde{r})$ shows a more rapid increase at small distances from the cylinder (condensed region), indicating a stronger accumulation of counterions near the cylinder surface. A similar trend has been observed in previous simulations [25,74–76] and in experiments with multivalent counterions [83]. It will be analyzed in more detail in the following sections.

However, the excessive accumulation of counterions near the cylinder for large Ξ does not imply a larger condensed fraction, because, as seen in Fig. 3, the *large-distance* behavior of the density profile is *not* influenced by electrostatic correlations and so remains the condensed fraction (plateau level) unaffected by increasing the coupling parameter. This is demonstrated by the condensed fraction data in the inset of Fig. 4. This result can be appreciated only when the asymptotic behavior for $\Delta\gg 1$ is considered.

3. Order parameter S_n

The nth-order inverse moment of the counterionic density profile may be calculated numerically using

$$S_n=\frac{1}{N}\sum_{i=1}^{N}\overline{\tilde{r}_i^{-n}} \tag{75}$$

for $n>0$, where $\tilde{r}_i$ is the radial distance of the ith counterion from the central cylinder axis and the overbar denotes the Monte Carlo (MC) time average after proper equilibration of the system. The global behavior of S_1 is shown in Fig. 5 as a function of the Manning parameter ξ. Recall that a vanishing order parameter $S_1=0$ indicates complete decondensation of counterions, while a finite $S_1>0$ reflects a finite degree of counterion binding (corresponding to a finite localization length $\sim 1/S_1$).

As seen from the figure, decondensation can occur in all relevant regimes of the coupling parameter Ξ. For large Manning parameter ξ, electrostatic coupling effects become important and shift the order parameter to larger values exhibiting a crossover from the mean-field prediction (solid curve), which is thus verified for small $\Xi<1$, to the strong-coupling prediction (dashed curve) at very large values of Ξ. The mean-field result follows from Eq. (40), and the strong-coupling prediction is obtained using Eq. (67). As seen, in the transition regime $\xi\sim 1$, the order parameter data remain close to the mean-field curve and deviate from the SC prediction. A close examination of the correlation effects as well as finite-size effects in this region is essential in analyzing the critical behavior and will be considered later. Here we concentrate on the correlation-induced crossover observed in the condensation phase (large ξ).

4. Electrostatic correlations for large ξ

In Fig. 6, we plot the simulated radial density profile of counterions, $\tilde{\rho}(\tilde{r})$, for $\xi=3.0$ and consider several different coupling parameters. In agreement with the preceding results, the counterionic density in the immediate vicinity of the charged cylinder increases with Ξ, exhibiting large deviations from the mean-field prediction. For a given surface charge density σ_s, the observed trend is predicted, e.g., for increasing counterion valency q, since the coupling parameter scales as $\Xi\sim q^3$ [Eq. (8)]. The crossover from the mean-field prediction (solid curve) to the strong-coupling prediction (dashed curve) appears to be quite weak, in agreement with the situation observed for counterions at planar charged walls [60]. These profiles are calculated from Eqs. (27) and (63), respectively, and both decay *algebraically* with the radial distance $\tilde{r}$. But the SC profile shows a faster decay and

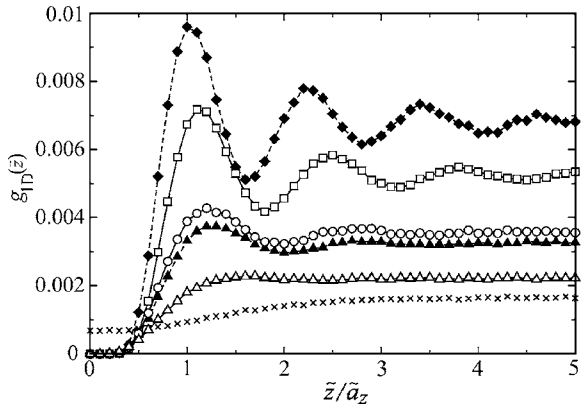

FIG. 7. The one-dimensional pair distribution function of counterions at contact with the cylinder as defined in Eq. (76). Symbols show the simulation data for $\Xi=10^5$ and $\xi=4.0$ (solid diamonds), $\Xi=10^3$ and $\xi=2.0, 3.0$, and 4.0 (open symbols from bottom to top) and for coupling parameters $\Xi=10$ and $\Xi=100$ with Manning parameter $\xi=3.0$ (cross symbols and solid up triangles respectively).

thus a more compact counterion layer near the cylinder for large Ξ [compare, e.g., Eqs. (34) and (65)].

An interesting point is that the simulated density at contact shows a more rapid increase when the coupling parameter increases from $\Xi=10$ to $\Xi=100$ as compared to other ranges of Ξ (Fig. 6). This is in fact accompanied by the formation of correlation holes around counterions near the surface as we show now.

In order to examine counterion-counterion correlations near the cylinder surface, we consider the one-dimensional pair distribution function of counterions, $g_{1D}(\tilde{z})$, which measures the probability of finding two counterions lined up along z axis (i.e., along the cylinder axis with equal azimuthal angles ϕ) at a distance $\tilde{z}$ from each other. In Fig. 7, we plot the unnormalized pair distribution function

$$g_{1D}(\tilde{z}) \equiv \frac{1}{N}\sum_{i\neq j} \langle \delta(\tilde{z}_i - \tilde{z}_j - \tilde{z})\,\delta(\phi_i - \phi_j)\rangle, \tag{76}$$

where the sum runs only over counterions at the surface (defined in the simulations as counterions residing in a shell of thickness about the Gouy-Chapman length μ around the cylinder). At small coupling ($\Xi=10$, cross symbols), the pair distribution function only shows a very weak depletion zone at small distances along the cylinder axis. For larger values of Ξ, one observes a pronounced correlation hole at small distances around counterions, where the distribution function vanishes over a finite range. This correlation hole develops in the range of coupling parameters, $10<\Xi<100$, which marks the crossover regime between the mean-field and strong-coupling regimes (compare cross symbols and solid up triangles). The correlation hole appears only at sufficiently large Manning parameter ξ (i.e., when there is a sufficiently large number of condensed counterions) and is distinguishable in our simulations for $\xi>1.2$.

The small-separation correlation hole is followed by an oscillatory behavior for elevated ξ indicative of a short-ranged liquidlike order among counterions lined up along the cylinder axis (distinguishable from the data for $\xi>2.0$ in the large-coupling regime $\Xi>100$). The location of the first peak of g_{1D} gives a rough measure of the typical distance between lined-up counterions, a_z, at the cylinder surface. This distance is set by the local electroneutrality condition $a_z\tau=q$. In rescaled units and using Eqs. (5), (6), and (8), we obtain

$$\tilde{a}_z \equiv \frac{a_z}{\mu} = \frac{\Xi}{\xi}, \tag{77}$$

which is used to rescale the horizontal axis in Fig. 7.

Note that the correlation hole size increases with the coupling parameter and thus counterions at the surface become highly isolated, reflecting dominant single-particle contributions for $\Xi \gg 1$ [59,60]. In fact, as discussed elsewhere [59–63,69], the single-particle form of the SC theory (derived formally in the limit $\Xi\to\infty$) is a direct consequence of large correlation holes around counterions at the surface. Clearly, for the counterion-cylinder system, this can be the case only for sufficiently large Manning parameter, where a sizable fraction of counterions can gather near the surface. Consequently in the condensation regime, the data tend to the strong-coupling predictions for elevated Ξ (Figs. 5 and 6) as also verified in the simulations of charged plates [60] (where all counterions are bound to the surface) and two charged cylinders with large ξ [61]. This also explains why the SC theory, though being able to reproduce the CCT on a qualitative level, fails to capture the quantitative features *near the critical point*, where counterions are mostly decondensed (except for the value of the critical Manning parameter, which is correctly reproduced).

B. Critical Manning parameter ξ_c

We now turn our attention to the critical behavior of counterions and begin with determining the precise location of the critical Manning parameter, ξ_c.

To this end, we employ a procedure similar to the method of locating the transition temperature in bulk critical phenomena [52,84]. Namely, we expect that the transition is reflected by a singular behavior in thermodynamic quantities such as energy or heat capacity as already indicated by the mean-field results obtained in Sec. III D. The (excess) internal energy E_N and the (excess) heat capacity C_N may be obtained directly from the simulations and in rescaled units as

$$\tilde{E} = \frac{E_N}{Nk_BT} = \left\langle \frac{\mathcal{H}_N}{Nk_BT} \right\rangle, \tag{78}$$

$$\tilde{C} = \frac{C_N}{Nk_B} = N\left\langle \left(\frac{\delta\mathcal{H}_N}{Nk_BT} \right)^2 \right\rangle, \tag{79}$$

where the configurational Hamiltonian $\mathcal{H}_N$ is defined through Eq. (10) and $\delta\mathcal{H}_N=\mathcal{H}_N-\langle\mathcal{H}_N\rangle$.

Simulation results for the rescaled energy $\tilde{E}$ and the rescaled heat capacity $\tilde{C}$ in Fig. 8 (symbols) show a nonmonotonic behavior as a function of ξ. The energy develops a

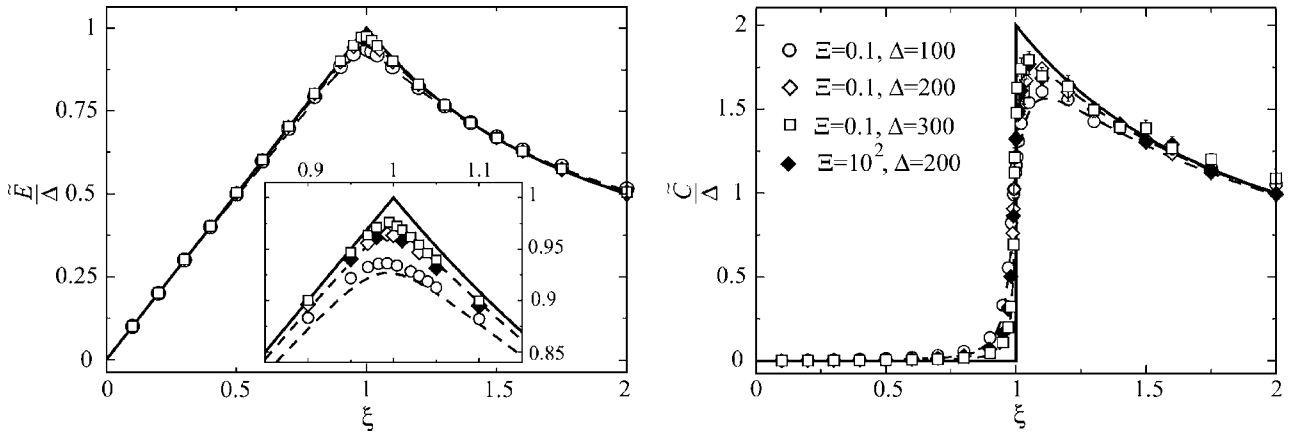

FIG. 8. (a) The rescaled internal energy $\tilde{E}=E_N/(Nk_BT)$ and (b) the rescaled heat capacity $\tilde{C}=C_N/(Nk_B)$ of the counterion-cylinder system as a function of the Manning parameter ξ. Open symbols show the simulation data for small coupling parameter $\Xi=0.1$ and lateral extension parameters $\Delta=100$, 200, and 300 as indicated on the graph. Solid symbols are the data for large coupling parameter $\Xi=10^2$ with $\Delta=200$. Number of counterions is $N=100$. Solid curves show the asymptotic PB prediction for $\Delta\to\infty$ [Eqs. (61) and (62)]. Dashed curves are the full PB results for $\Delta=100$ and 300 (from bottom to top), which are calculated numerically using Eqs. (59) and (81). The inset shows a closer view of the energy peak.

pronounced peak, and the heat capacity exhibits a jump at intermediate Manning parameters, which become singular for $\Delta\to\infty$. The global behavior of these quantities can be understood using simple arguments as follows.

For sufficiently small ξ, counterions are all unbound and the electrostatic potential in space is roughly given by the bare potential of the charged cylinder—i.e., $\psi(\tilde{r}) \simeq 2\xi \ln(\tilde{r}/\tilde{R})$. This yields the rescaled internal energy $\tilde{E}$ [via integrating the squared electric field, Eq. (58)] as

$$\tilde{E}=\frac{1}{4\xi}\int_{\tilde{R}}^{\tilde{D}}\tilde{r}\,d\tilde{r}\left(\frac{d\psi}{d\tilde{r}}\right)^2\simeq\xi\Delta, \tag{80}$$

when $\Delta=\ln(D/R)\gg 1$. Intuitively, this result may be obtained also by assuming that counterions experience the potential of the cylinder at the outer boundary; thus, one simply has $\tilde{E}\simeq\psi(\tilde{D})/2\simeq\xi\Delta$, which explains the linear increase of the left tail of the energy curve with both ξ and Δ [Fig. 8(a)]. Now using the thermodynamic relation

$$\xi\frac{\partial\tilde{E}}{\partial\xi}=\tilde{E}-\tilde{C}, \tag{81}$$

the excess heat capacity is obtained to vanish in the decondensation phase—i.e., $\tilde{C}\simeq 0$ [Fig. 8(b)]. Hence, the total heat capacity reduces to that of an ideal gas of particles.

For large ξ, the electrostatic potential of the cylinder is screened due to counterionic binding. If we estimate the screened electrostatic potential of the cylinder as $\psi(\tilde{r}) \simeq 2\ln(\tilde{r}/\tilde{R})$, which can be verified systematically within the PB theory [10,54,70], we obtain the energy and the heat capacity as

$$\tilde{E}\simeq\Delta/\xi,\quad \tilde{C}\simeq 2\Delta/\xi. \tag{82}$$

These results may also be obtained by noting that only decondensed counterions (Sec. VI A 2) contribute to the energy on the leading order; thus, $\tilde{E}\simeq\psi(\tilde{D})/(2\xi)\simeq\Delta/\xi$. The above asymptotic estimates in fact coincide with the asymptotic ($\Delta\to\infty$) PB results (61) and (62), which are shown by solid curves in Fig. 8.

The preceding considerations demonstrate that the nonmonotonic behavior of the energy and heat capacity results directly from the screening effect due to condensation of counterions as ξ increases. Hence, the singular peaks emerging in both quantities should give the threshold of the counterion-condensation transition, ξ_c, in the thermodynamic infinite-system-size limit ($N\to\infty$ and $\Delta\to\infty$). Within the PB theory (solid and dashed curves in Fig. 8), the location of the peak of energy, $\xi_*^{E,\mathrm{PB}}(\Delta)$, tends to the mean-field critical value $\xi_c^{\mathrm{PB}}=1$ from *below* as Δ increases, obeying the finite-size-scaling relation

$$\xi_c^{\mathrm{PB}}-\xi_*^{E,\mathrm{PB}}(\Delta)\simeq\frac{1}{\Delta}, \tag{83}$$

which is obtained using the full PB energy (59). On the other hand, the location of the peak of the PB heat capacity approaches ξ_c^{PB} from *above*.

We locate the critical point from the asymptotic behavior of the energy peak ξ_*^E as N and Δ increase. (The heat capacity peak is found to be located farther away from the critical point as compared to the energy peak, resembling the well-known behavior of the heat capacity peak in finite magnetic systems [84,85]; it is therefore inconvenient for our purposes.) In Fig. 9, we show the simulation results for ξ_*^E (symbols) as a function of Δ^{-1} for $\Xi=0.1$ and various number of particles (main set). These data are obtained using the thermodynamic relation (81), which enables one to calculate the first derivative of energy, $\partial\tilde{E}/\partial\xi$, directly from the energy and the heat capacity data without making use of numerical differentiation methods that typically generate large errors near a maximum. As N increases, the data converge to and closely follow the mean-field prediction (solid curve) within

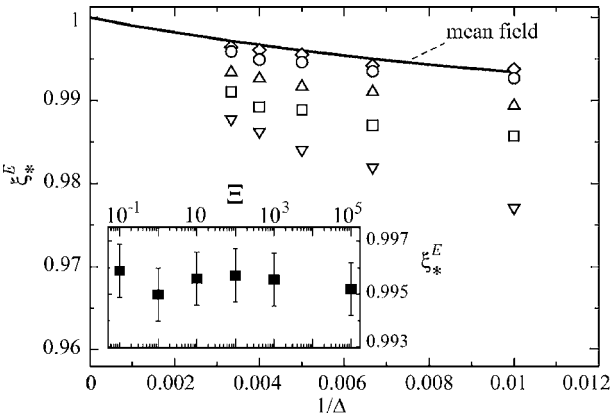

FIG. 9. Main set: location of the peak of energy, ξ_*^E, as a function of the inverse lateral extension parameter, $1/\Delta=[\ln(D/R)]^{-1}$. Open symbols are the simulation data for small coupling parameter $\Xi=0.1$ and different number of counterions (from bottom): $N=25$ (down triangles), 50 (squares), 100 (up triangles), 200 (circles), and 300 (diamonds). Solid curve shows the mean-field prediction for the peak location obtained by numerical evaluation of the full PB energy, Eq. (59). Inset: location of the simulated energy peak as a function of the coupling parameter Ξ for $N=200$ and $\Delta=300$.

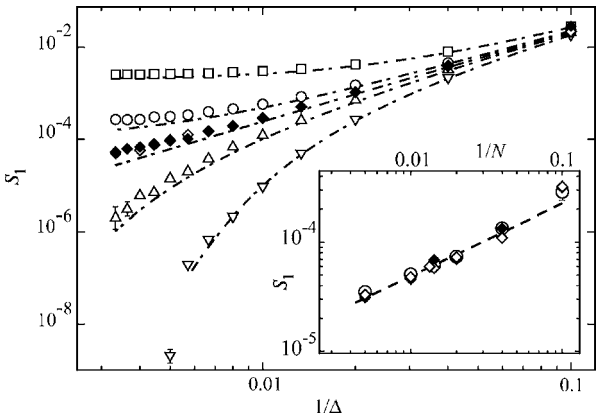

FIG. 10. Main set: order parameter $S_1=\langle 1/\tilde{r}\rangle$ as a function of the inverse lateral extension parameter $1/\Delta$. Open symbols are the simulation data for $\Xi=0.1$ and Manning parameters (from top): $\xi=1.05$ (squares), 1.01 (circles), 1.0 (open diamonds), 0.99 (up triangles), and 0.97 (down triangles). Solid diamonds are the data for large coupling parameter $\Xi=10^2$ and $\xi=1.0$. Number of counterions, $N=100$, is fixed. Dot-dashed curves are the PB result (40) for the corresponding ξ. Inset: simulated S_1 as a function of the inverse number of counterions, $1/N$, for $\xi=1.0$, $\Delta=300$, and coupling parameters $\Xi=0.1$ (open diamonds), 10^2 (solid diamonds), and 10^3 (open circles). Dashed line shows the power law $S_1\sim N^{-2/3}$.

the simulation error bars; for $N>100$, ξ_*^E lies within about 1% of the PB critical Manning parameter $\xi_c^{\mathrm{PB}}=1$.

Since in the simulations we have used $\Delta\leqslant 300$, the behavior of ξ_*^E for very small $\Delta^{-1}\to 0$ is not obtained; nevertheless, the excellent convergence of the data for $\Xi=0.1$ to the PB prediction gives an accurate estimate for the critical Manning parameter as

$$\xi_c = 1.000 \pm 0.002. \tag{84}$$

Our results for larger values of the coupling parameter Ξ in the inset of Fig. 9 show that the location of the energy peak does not vary with the coupling parameter. Therefore, the critical Manning parameter is *universal* and agrees with the mean-field value $\xi_c=1.0$. Recall that the same threshold is obtained within the strong-coupling theory (Sec. IV).

Another important result is that the CCT is not associated with a diverging singularity in contrast to the Onsager instability prediction [1]. But the energy at any finite value of ξ and, also, the heat capacity for $\xi>1$ tend to infinity (as $\sim\Delta$) when the lateral extension parameter Δ increases to infinity. As discussed above, this reflects the logarithmic divergency of the effective electrostatic potential in a charged cylindrical system.

Note also that the CCT exhibits a *universal* jump $\delta\tilde{C}$ in the limiting heat capacity at ξ_c [Fig. 8(b)]—i.e.,

$$\lim_{\Delta\to\infty}\frac{\delta\tilde{C}}{\Delta}=2. \tag{85}$$

It thus represents a second-order phase transition.

C. Scale invariance near the critical point

Now that the precise location of the critical Manning parameter is determined, a finite-size analysis, similar to what we presented within mean-field theory, may be used to determine the scaling properties of the CCT order parameters from the simulation data.

Note that in the simulations, finite-size effects arise both from the finiteness of the system size (via the lateral extension parameter Δ) and also from the finiteness of the number of counterions, N, the latter being related to the finiteness of the height of the main simulation box $L=Nq/\tau$ (Sec. V), which has a sizable influence on the transition, although the implemented periodic boundary condition in the z direction already reduces its effects. In what follows, we present the numerical evidence for scaling relations with respect to both N and Δ. The asymptotic finite-size behavior as N and Δ increase to infinity provides us with the scaling exponent associated with the reduced Manning parameter ζ (or the reduced temperature t), identifying the CCT universality class in 3D.

1. Finite-size effects near ξ_c

In Fig. 10 (main set), we show the order parameter S_1 (mean inverse localization length of counterions) as a function of $1/\Delta$ and in the vicinity of the critical point $\xi_c=1$ (number of counterions, $N=100$, is fixed). As seen, S_1 gradually decreases with decreasing $1/\Delta$ as decondensation of counterions becomes gradually more pronounced. But for Manning parameters as large as $\xi=1.05$ (squares), the data quickly saturate to a finite value as $\Delta\to\infty$. For sufficiently small Manning parameter (e.g., $\xi<0.97$), on the other hand, S_1 converges to zero. In the vicinity of the critical point ($\xi=1$, diamonds), a nonsaturating behavior is found, suggesting a power-law decay as $S_1\sim\Delta^{-\gamma}$, where $\gamma>0$. The data at $\xi=1$ roughly coincide for both small coupling parameter ($\Xi=0.1$, open diamonds) and large coupling parameter

($\Xi=10^2$, solid diamonds), indicating that electrostatic correlations do not influence the scaling behavior (Sec. VI D below). There still remain non-negligible deviations between the simulation data at the critical point (diamonds) and the PB power-law prediction (45), which is characterized by the exponent $\gamma_{\mathrm{PB}}=2$ (shown in the figure by a straight dot-dashed line). These deviations arise from the finiteness of the number of particles.

Interestingly, the data obtained for various number of counterions, N (at fixed lateral extension parameter Δ), also indicate a power-law decay near the critical point as $S_1 \sim N^{-\nu}$, where $\nu>0$. This is shown in the inset of Fig. 10, where the scaling exponent ν appears to be about 2/3 (represented by a dashed line). In fact, for sufficiently large N, the data deviate from this power-law behavior as the finite-size effects due to the lateral size of the system are simultaneously present (data not shown). Thus, in order to determine the exponents γ and ν, a more systematic approach is required, which should incorporate both lateral-size and ion-number effects.

2. Generalized finite-size scaling

In brief, our data suggest that at the critical point ($\zeta=\zeta_c=0$) and for a bounded system (finite Δ) in the thermodynamic limit $N\to\infty$, the order parameter $S_n(\zeta,\Delta,N)=\langle 1/\tilde{r}^n\rangle$ decays as

$$S_n(0,\Delta,\infty)\sim\Delta^{-\gamma}, \tag{86}$$

while in an infinite system ($\Delta\to\infty$) with finite number of particles, N, it decays as

$$S_n(0,\infty,N)\sim N^{-\nu}. \tag{87}$$

In the thermodynamic infinite-system-size limit ($N\to\infty$ and $\Delta\to\infty$), the critical transition sets in with $S_n(\zeta<0,\infty,\infty)=0$, and we anticipate a scaling behavior with the reduced Manning parameter $\zeta=1-\xi_c/\xi$ as

$$S_n(\zeta,\infty,\infty)\sim\zeta^{\chi} \tag{88}$$

in a sufficiently small neighborhood *above* $\xi_c=1$.

These scaling relations may all be deduced from a general finite-size-scaling hypothesis for S_n—i.e., by assuming that $S_n(\zeta,\Delta,N)$ takes a *homogeneous scale-invariant* form with respect to its arguments in the vicinity of the transition point ξ_c when both N and Δ are sufficiently large. In other words, for any positive number $\lambda>0$,

$$S_n(\lambda\zeta,\lambda^{-b}\Delta,\lambda^{-c}N)=\lambda^a S_n(\zeta,\Delta,N), \tag{89}$$

where a, b, and c are a new set of exponents associated with ζ, Δ, and N, respectively. The above relation implies that when the reduced Manning parameter ζ is rescaled with a factor λ, the size parameters N and Δ can be rescaled such that the order parameter remains invariant up to a scaling prefactor. Finite-size scale invariance is a common feature in critical phase transitions [52,86] and provides an accurate tool to estimate critical exponents in numerical simulations [84,85]. The exponents in Eq. (89) can be calculated directly from MC simulations. These exponents are related to and give the values of the desired critical exponents γ, ν, and χ, as will be shown below. Note that these exponents may in general depend on n (the index of S_n), the coupling parameter Ξ, and the space dimension, which are not explicitly incorporated in the proposed scaling hypothesis, but their influence will be examined later.

Given Eq. (89), the following relations are obtained by suitably choosing λ. For $\lambda=N^{1/c}$, one finds

$$S_n(\zeta,\Delta,N)=N^{-a/c}\mathcal{C}_n(\zeta N^{1/c},\Delta N^{-b/c}), \tag{90}$$

where $\mathcal{C}_n(u,v)$ is the scaling function corresponding to a system with both finite N and Δ. The above expression is useful for a system with finite N in the limit $\Delta\to\infty$. Thus, assuming that $\mathcal{C}_n(u,v)$ exists for $v=\Delta N^{-b/c}\to\infty$, the relation (90) reduces to

$$S_n(\zeta,\infty,N)=N^{-a/c}\mathcal{N}_n(\zeta N^{1/c}), \tag{91}$$

where the scaling function $\mathcal{N}_n(u)=\mathcal{C}_n(u,\infty)$. The critical exponent ν follows by considering this relation right at the critical point, $\zeta=0$—i.e.,

$$S_n(0,\infty,N)=\mathcal{N}_n(0)N^{-\nu}, \tag{92}$$

where ν is obtained as

$$\nu=\frac{a}{c}. \tag{93}$$

On the other hand, we assume that in the vicinity of the critical point, $S_n(\zeta,\infty,N)$ is a finite function of only the reduced Manning parameter ζ when the limit $N\to\infty$ is taken. Hence the scaling function $\mathcal{N}_n(u)$ is required to behave as $\mathcal{N}_n(u)\sim u^a$ for $u\to\infty$, which yields

$$S_n(\zeta,\infty,\infty)\sim\zeta^{\chi}, \tag{94}$$

where the critical exponent associated with ζ reads

$$\chi=a. \tag{95}$$

To determine the critical exponent associated with Δ in terms of the exponents $\{a,b,c\}$, we need to consider Eq. (89) for $\lambda=\Delta^{1/b}$. We thus have

$$S_n(\zeta,\Delta,N)=\Delta^{-a/b}\mathcal{C}'_n(\zeta\Delta^{1/b},N\Delta^{-c/b}), \tag{96}$$

where $\mathcal{C}'_n(u,v)$ is a new scaling function. This relation is useful for a system with finite Δ in the limit $N\to\infty$, where assuming that $\mathcal{C}'_n(u,v)$ exists, we obtain

$$S_n(\zeta,\Delta,\infty)=\Delta^{-a/b}\mathcal{D}_n(\zeta\Delta^{1/b}), \tag{97}$$

with a new scaling function $\mathcal{D}_n(u)=\mathcal{C}'_n(u,\infty)$. The critical exponent γ follows by considering this relation right at the critical point $\zeta=0$, which yields

$$S_n(0,\Delta,\infty)=\mathcal{D}_n(0)\Delta^{-\gamma}, \tag{98}$$

where γ reads

$$\gamma = \frac{a}{b}. \tag{99}$$

Therefore, we have a complete set of relations (93), (95), and (99) from which the critical exponents γ, ν, and χ may be obtained using the exponents a, b, and c. (We have assumed that these exponents are positive as will be verified later.)

Equation (97) compares directly with the mean-field result (48) in Sec. III C, where we showed that $\gamma_{\mathrm{PB}}=2$ and $\chi_{\mathrm{PB}}=2$. Recall that the exponent ν is not defined within mean-field theory.

D. Critical exponents: The CCT universality class

1. Exponents χ and ν

In order to verify the generalized finite-size-scaling hypothesis (89) and estimate the critical exponents numerically, we adopt the standard data-collapse scheme [84].

We begin with the exponents χ and ν, which can be calculated using Eq. (90), which involves a scaling function $\mathcal{C}_n(u,v)$ of two arguments $u=\zeta N^{1/c}$ and $v=\Delta N^{-b/c}$. In our simulations, N ranges from 25 up to 300 and Δ from 50 up to 300; thus, assuming that the exponent b/c is small, which will be verified later, we deal with a typically large value for $v\sim 10-10^2$. Therefore the limiting relation (91) is approximately valid and yields

$$N^{a/c}S_n \simeq \mathcal{N}_n(\zeta N^{1/c}). \tag{100}$$

Now if the simulation data for S_n are plotted as a function of $\zeta=1-\xi_c/\xi$ for *various* N (but at fixed sufficiently large Δ), Eq. (100) predicts that by rescaling the reduced Manning parameter ζ by the factor $N^{1/c}$ and the order parameter by the factor $N^{a/c}$, all data should collapse onto a single curve. Numerically, this procedure allows us to determine the exponents a/c and $1/c$ in such a way that the best data collapse is achieved within the simulation error bars. We show the results for S_1 in Fig. 11 for various N and the coupling parameter $\Xi=0.1$ (main set). The collapse of the data onto each other is indeed achieved within the numerical error bars for exponents in the range $1/c\simeq 1/3\pm 0.05$ and $a/c\simeq 2/3\pm 0.1$. This yields the critical exponents ν and χ from Eqs. (93) and (95) as

$$\nu \simeq 2/3 \pm 0.1, \tag{101}$$

$$\chi \simeq 2.0 \pm 0.4, \tag{102}$$

where the errors are estimated using the standard error-propagation methods. The value obtained for χ agrees with the mean-field result, Eq. (44).

In order to check whether the exponents vary with the electrostatic coupling parameter Ξ, we repeat this procedure for a wide of range of values for Ξ. We find the same values for the exponents χ and ν for coupling parameters up to $\Xi=10^5$. For comparison, the results for $\Xi=10^3$ are shown in the inset of Fig. 11, where the data collapse is demonstrated using $1/c=1/3$ and $a/c=2/3$.

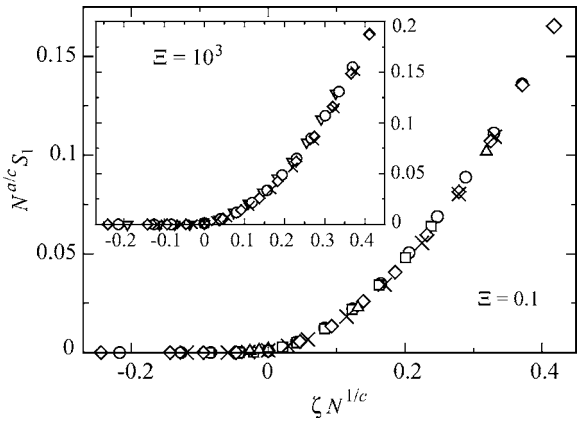

FIG. 11. Rescaled order parameter $N^{a/c}S_1$ as a function of the rescaled reduced Manning parameter $\zeta N^{1/c}$ in the vicinity of the critical point $\xi_c=1.0$ for small and large coupling parameters $\Xi=0.1$ (main set) and $\Xi=10^3$ (inset). Symbols show the simulation data for various number of particles $N=50$ (down triangles), 70 (circles), 75 (squares), 100 (diamonds), 200 (cross symbols), and 300 (up triangles) at fixed $\Delta=300$. Here, the exponents are chosen as $a/c=2/3$ and $1/c=1/3$. Error bars are smaller than the symbol size.

2. Exponent γ

Given the exponents a and c as determined above and making use of the finite-size-scaling relation (96), we can estimate the exponent b and, thereby, the scaling exponent γ associated with the lateral extension parameter Δ. In this case, however, the second argument $v=N\Delta^{-c/b}$ in the scaling function $\mathcal{C}'_n(u,v)$ in Eq. (96) may not be considered as large within our simulations (since, as shown below, the ratio c/b is large). But it turns out that the dependence of $\mathcal{C}'_n(u,v)$ on v is quite weak such that the finite-size-scaling relation (97) is approximately valid and can be used to determine the desired exponent. To examine this latter property of $\mathcal{C}'_n(u,v)$, we consider relation (96) right at the critical point $(\zeta=\zeta_c=0)$—i.e.,

$$S_n(0,\Delta,N) = \Delta^{-a/b}\mathcal{C}'_n(0,N\Delta^{-c/b}). \tag{103}$$

In Fig. 12 (main set), $S_1(0,\Delta,N)$ is plotted as a function of Δ in a log-log plot for increasing N from 70 up to 300 and for $\Xi=0.1$. As clearly seen, the order parameter varies quite weakly with the number of particles and the variations are already within the error bars (equal to or smaller than the symbol size) for $N>100$.

Thus multiplying both sides of Eq. (97) with $\Delta^{a/b}$, we have

$$\Delta^{a/b}S_n \simeq \mathcal{D}_n(\zeta\Delta^{1/b}), \tag{104}$$

in which the exponent a is previously determined as $a=\chi=2.0\pm 0.4$. We thus plot the order parameter S_n as a function of ζ for *various* Δ (but at fixed sufficiently large N) and rescale S_n and ζ by the scaling factors $\Delta^{a/b}$ and $\Delta^{1/b}$, respectively; the exponent b is chosen such that the best data collapse is obtained within the error bars. The results are shown in Fig. 13 for $\Delta^{a/b}S_1$ as a function of $\zeta\Delta^{1/b}$, where the coupling parameter is chosen as $\Xi=0.1$ (main set). The collapse

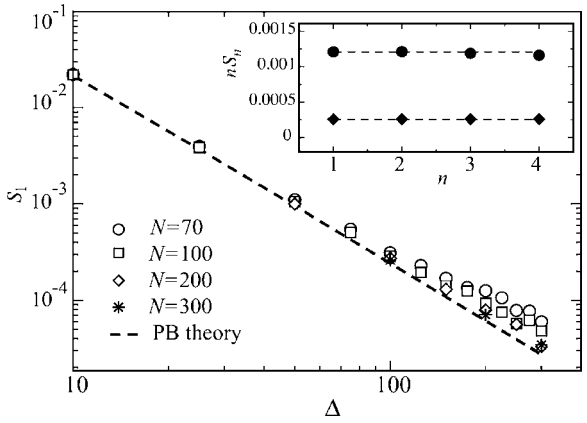

FIG. 12. Main set: simulated order parameter S_1 as a function of the lateral extension parameter Δ for increasing number of counterions from $N=70$ up to 300 as indicated on the graph (Manning parameter is $\xi=1.0$ and the coupling parameter $\Xi=0.1$). Dashed line shows the PB power law, Eq. (45). Inset: rescaled order parameter $S_n=\langle 1/\tilde{r}^n\rangle$ as a function of the index n for Manning parameters close to the critical value (from top): $\xi=1.03$ (solid circles) and $\xi=1.01$ (solid diamonds). Here, the coupling parameter is $\Xi=0.1$, number of counterions is $N=100$, and $\Delta=300$.

of the data onto each other is obtained only for the exponent $1/b$ in the range $1/b\simeq 1.0\pm 0.2$, yielding the critical exponent γ, Eq. (99), as

$$\gamma \simeq 2.0 \pm 0.6, \tag{105}$$

which agrees with the mean-field exponent, Eq. (47). We find the same value for γ by repeating the above procedure for larger coupling parameters. For instance, the results for $\Xi=10^5$ are shown in the inset of Fig. 13, where we have chosen $1/b=1.0$ and $a/b=2.0$.

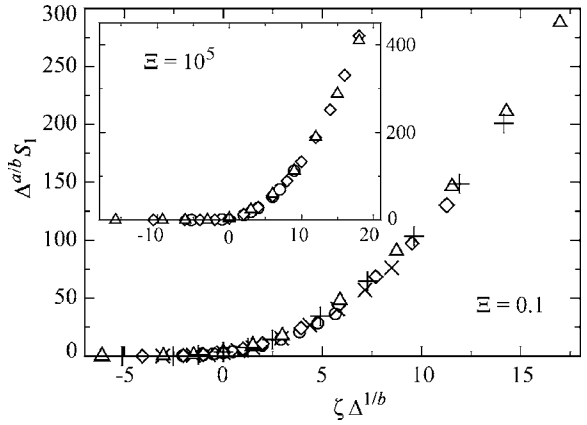

FIG. 13. Rescaled order parameter $\Delta^{a/b}S_1$ as a function of the rescaled reduced Manning parameter $\zeta\Delta^{1/b}$ in the vicinity of the critical point $\xi_c=1.0$ for small and large coupling parameters $\Xi=0.1$ (main set) and $\Xi=10^5$ (inset). Symbols show the simulation data for various lateral extension parameters $\Delta=100$ (circles), 150 (cross symbols), 200 (diamonds), 250 (plus symbols), and 300 (up triangles). Number of counterions is fixed ($N=200$ for the coupling parameter $\Xi=0.1$ and $N=100$ for $\Xi=10^5$), and the exponents are chosen here as $a/b=2.0$ and $1/b=1.0$.

Note that the estimated values of b and c show that the ratio b/c is as small as 1/3, which is consistent with the assumption made in the foregoing data-collapse procedure.

As a main result, our numerical data confirm the existence of critical scaling relations associated with the counterion-condensation transition in 3D and show that the values of the critical exponents are *universal*; i.e., they are independent of the coupling parameter Ξ and fall within the mean-field universality class.

Also, in agreement with the mean-field results, the exponents are found to be independent of n, the index of the order parameters $S_n=\langle 1/\tilde{r}^n\rangle$. In fact, we find that the higher-order moments are related to the first-order moment S_1 via

$$S_n \simeq \frac{S_1}{n} \tag{106}$$

in the *vicinity* of the critical point. This indicates that nS_n is independent of n as demonstrated in the inset of Fig. 12 [compare with the mean-field relation (41)].

VII. COUNTERION-CONDENSATION TRANSITION IN TWO DIMENSIONS

In this section, we investigate the role of space dimension in the unbinding behavior of counterions near a charged cylinder by considering a 2D counterion-cylinder model. As a typical trend in bulk critical phenomena, effects of fluctuations near a critical point are expected to grow with diminishing dimension [52], leading to large deviations from mean-field theory. It is therefore interesting to examine the CCT in a lower spatial dimension.

A. Two-dimensional model

In 2D, we use a primitive cell model similar to the 3D model described in Sec. II A. It consists of a 2D central charged cylinder (central "disk") of radius R confined coaxially and together with its neutralizing pointlike counterions in an outer cylinder (outer "ring") of radius D. In order to construct the interaction Hamiltonian, we use the fact that the Coulomb interaction between two elementary charges in 2D (the 2D Green's function) is of the form

$$v_{2D}(\mathbf{x}) = -\ln|\mathbf{x}|. \tag{107}$$

This follows directly from the solution of the 2D Poisson equation for a point charge—that is,

$$\nabla^2 v_{2D}(\mathbf{x}) = -2\pi\delta^2(\mathbf{x}). \tag{108}$$

The configurational Hamiltonian of the 2D system may thus be written as

$$\frac{\mathcal{H}_N}{k_BT} = \lambda_c\lambda_r\sum_{i=1}^{N}\ln\left(\frac{r_i}{R}\right) - \lambda_c^2\sum_{\langle ij\rangle}\ln\left|\frac{\mathbf{x}_i-\mathbf{x}_j}{R}\right|, \tag{109}$$

with $\mathbf{x}_i=(r_i,\phi_i)$ being the position vector of the ith counterion (in polar coordinates) and λ_c and λ_r being the dimensionless charges of the counterions and the cylinder, respectively. The first term gives the counterion-cylinder attraction, and the second term gives mutual repulsions between counteri-

ons. Clearly, the present 2D model is equivalent to a 3D system comprising an infinite central cylinder and mobile *parallel* lines of opposite charge ("counterions"). It may be applicable to a system of oriented cationic and anionic polymers [64–67].

Taking the logarithmic interaction as in Eq. (107) will also ensure that the general form of the field-theoretic representation of the partition function remains the same as in the 3D case [72] and, in particular, that the mean-field Poisson-Boltzmann theory, which follows from a saddle-point analysis, is given exactly by the same equations and results as discussed in Sec. III.

B. Rescaled representation

In analogy with the 3D system, the dimensionless *Manning parameter* ξ and the *coupling parameter* Ξ are defined as

$$\xi = \lambda_c \lambda_r / 2, \tag{110}$$

$$\Xi = \lambda_c^2 / 2. \tag{111}$$

These definitions can be justified systematically when the Hamiltonian of the system is mapped to an effective field theory, where Ξ and ξ formally appear in the same roles as in 3D [46]. We shall conventionally rescale the spatial coordinates as $\tilde{\mathbf{x}} = \mathbf{x}/\mu_{2D}$ using the 2D analog of the Gouy-Chapman length $\mu_{2D} \equiv R/\xi$ [see Eq. (7)]. The Hamiltonian in rescaled units reads

$$\frac{\mathcal{H}_N}{k_B T} = 2\xi \sum_{i=1}^{N} \ln\left(\frac{\tilde{r}_i}{\tilde{R}}\right) - 2\Xi \sum_{\langle ij \rangle} \ln \left| \frac{\tilde{\mathbf{x}}_i - \tilde{\mathbf{x}}_j}{\tilde{R}} \right|. \tag{112}$$

The electroneutrality condition implies $\lambda_r = N\lambda_c$, where N is the number of counterions in the system. This relation may also be written as

$$\xi = N\Xi. \tag{113}$$

Thus an important consequence of electroneutrality in 2D is that the coupling parameter and the Manning parameter are related only via the number of counterions. In particular, in the thermodynamic limit $N \to \infty$, the coupling parameter tends to zero, $\Xi \to 0$, suggesting that mean-field theory becomes *exact* for any finite ξ.

C. Centrifugal sampling

We use a similar simulation method as devised for the 3D system using the transformed coordinates (y, ϕ) with $y = \ln(\tilde{r}/\tilde{R})$ being the logarithmic radial distance of particles from the central cylinder. As explained in Sec. V, this transformation leads to the centrifugal sampling method appropriate for equilibration of a system with large lateral extension parameter $\Delta = \ln(D/R) \gg 1$. The 2D partition function thus reads

$$\mathcal{Z}_N = \frac{R^{2N}}{N!} \int_{\tilde{V}} \left[\prod_{i=1}^{N} d\phi_i \, dy_i \right] \exp\left\{ -\frac{\mathcal{H}_N^*}{k_B T} \right\}, \tag{114}$$

where $0 \leqslant y \leqslant \Delta$ and the transformed Hamiltonian

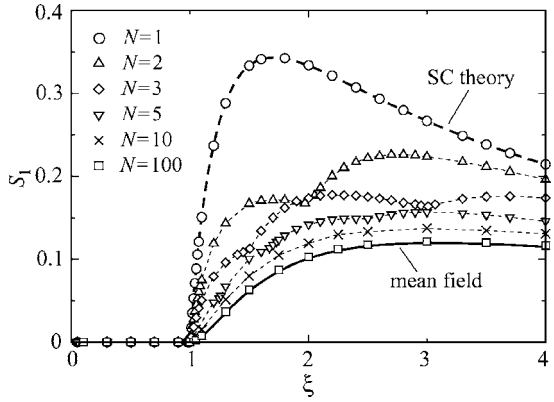

FIG. 14. Order parameter $S_1 = \langle 1/\tilde{r} \rangle$ as a function of the Manning parameter ξ for the 2D counterion-cylinder system. Symbols show the simulation data for different number of particles as indicated on the graph. The mean-field (solid) and the strong-coupling (dashed) curves are obtained from Eqs. (40) and (67), respectively, which are valid in 2D as well. The lateral extension parameter here is $\Delta = 300$. Thin dashed curves are guides to the eyes.

$$\frac{\mathcal{H}_N^*}{k_B T} = (2\xi - 2) \sum_{i=1}^{N} y_i - 2\Xi \sum_{\langle ij \rangle} \ln \left| \frac{\tilde{\mathbf{x}}_i - \tilde{\mathbf{x}}_j}{\tilde{R}} \right|. \tag{115}$$

The minimal set of dimensionless parameters in 2D is given by the Manning parameter ξ, number of counterions, N, and the lateral extension parameter Δ. The range of simulation parameters and other details are consistent with those given in Sec. V B.

VIII. SIMULATION RESULTS IN 2D

A. Order parameters

We consider the same set of order parameters $S_n = \langle 1/\tilde{r}^n \rangle$ as defined in Eq. (38) to characterize the CCT in 2D. They can be measured in the simulations as

$$S_n = \frac{1}{N} \sum_{i=1}^{N} \overline{\tilde{r}_i^{-n}} \tag{116}$$

for $n > 0$, where the overbar denotes the MC time average after proper equilibration of the system. Of particular interest is the behavior of S_n as a function of the Manning parameter ξ. It identifies the two regimes of complete decondensation (with $S_n = 0$) and partial condensation (with $S_n > 0$) when $\Delta \to \infty$. Unlike in 3D, where Ξ can be varied as an independent parameter, various coupling regimes in 2D are spanned by changing the number of particles, N, for a given ξ [see Eq. (113)].

The 2D simulation results for the order parameter S_1 are shown in Fig. 14 for various number of particles $N = 1$, 2, 3, 5, 10, and 100 (symbols) and for a large lateral extension parameter $\Delta = 300$. As seen for $N = 1$, the data trivially follow the strong-coupling prediction, Eq. (67), shown by the dashed curve (Sec. IV). As N increases, S_1 decreases, and for sufficiently large N, it converges to the mean-field PB prediction, Eq. (40), shown by the solid curve. This in fact oc-

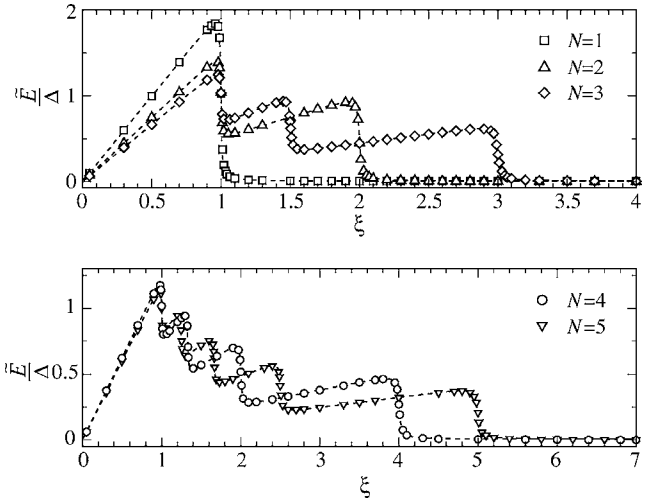

FIG. 15. The rescaled internal energy of the 2D counterion-cylinder system, $\widetilde{E}=E_N/(Nk_BT)$, as a function of the Manning parameter ξ for $\Delta=300$ and different number of particles as indicated on the graph. Symbols show the simulation data, and dashed curves are the analytical results obtained from Eq. (125). Singular regions represent successive condensation (decondensation) of counterions.

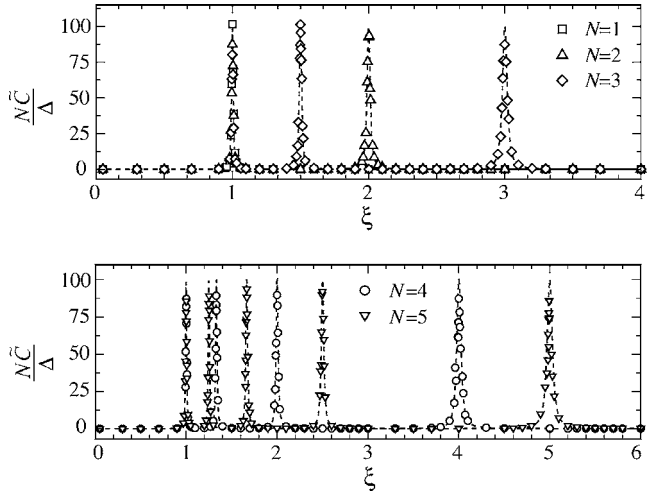

FIG. 16. The rescaled heat capacity of the 2D system, $\widetilde{C}=C_N/(Nk_B)$, as a function of the Manning parameter ξ for $\Delta=300$ and different number of particles, N, as indicated on the graph (for clarity, the data are multiplied by N). Symbols show the simulation data, and dashed curves are the analytical results obtained from Eq. (126). The peaks represent successive condensation (decondensation) of counterions.

curs for the whole range of Manning parameters and confirms the trend predicted from the 2D electroneutrality condition (113). Accordingly, scaling analysis of the order parameters for large N gives identical results for the critical exponents as in 3D (Secs. VI C and VI D) and agrees with mean-field theory. We shall not discuss it here any further.

The result that mean-field theory for the counterion-cylinder system is *exact* in 2D for $N\to\infty$ is in striking contrast with the typical situation in bulk phase transitions [52] and also with the results we obtained in 3D that reflect strong correlation effects in the condensation phase ($\xi>1$) for growing Ξ (see Sec. VI A 4).

The order-parameter data in Fig. 14, on the other hand, reveal a peculiar set of cusplike singularities that are quite pronounced for small number of particles. These points become strictly singular in the limit $\Delta\to\infty$ and represent the Manning parameters at which individual counterions successively condense (or decondense). We will demonstrate this point using an analytical approach in Sec. VIII C. (A similar singular behavior is found in 3D for small N, but it appears to be more complex and will not be considered in this paper.)

B. Energy and heat capacity

The singularities found in the order parameter at small N show up also in the internal energy and the heat capacity of the system. In Figs. 15 and 16, we plot the rescaled (excess) internal energy $\widetilde{E}=E_N/(Nk_BT)$ and the rescaled (excess) heat capacity $\widetilde{C}=C_N/(Nk_B)$ obtained from the simulations using Eqs. (78) and (79) and the 2D Hamiltonian (112), as a function of ξ for $N=1$, 2, 3, 4, and 5. As seen, the energy curve shows a sawtoothlike structure consisting of wide regular regions, in which the energy almost linearly increases, and narrow singular regions, where the energy rapidly drops (with a diverging slope). Recalling the thermodynamic relation

$$\xi\frac{\partial\widetilde{E}}{\partial\xi}=\widetilde{E}-\widetilde{C}, \tag{117}$$

it follows that the heat capacity vanishes in the regular regions, but exhibits highly localized peaks in the singular regions as seen in the simulation data in Fig. 16.

C. Condensation singularities in 2D: An analytical approach

In what follows, we present an approximate asymptotic analysis of the 2D partition function in the limit $\Delta\to\infty$, which elucidates the physical mechanism behind the singular behavior in 2D. A rigorous analysis of the 2D problem is still missing, and more systematic approximations have been developed very recently [46].

1. Partition function

Suppose that the Manning parameter is such that $N-m$ counterions are firmly bound to the central cylinder, while m counterions have decondensed to infinity, where $m=1,\ldots,N$. Using the 2D Hamiltonian (112), the partition function can exactly be written as

$$\mathcal{Z}_N=\int\left[\prod_{i=m+1}^{N}d\mathbf{x}_i\right]\exp\left\{-\frac{\mathcal{H}_{N-m}}{k_BT}\right\}\prod_{l=1}^{m}\mathcal{Z}_N^{(l)} \tag{118}$$

in actual units, where $\mathcal{H}_{N-m}$ represents interactions among condensed counterions (labeled by $i=m+1,\ldots,N$) and

TABLE I. Numerical values of the singular Manning parameters in 2D, Eq. (122), for different number of particles, N.

N	$\{\xi_N^s,\ldots,\xi_1^s\}$				
1	1				
2	1	2			
3	1	3/2	3		
4	1	$4/3\simeq 1.33$	2	4	
5	1	$5/4=1.25$	$5/3\simeq 1.67$	5/2	5

$$\mathcal{Z}_N^{(l)} = \int d\mathbf{x}_l \exp\left\{ -2\xi \ln\left(\frac{r_l}{R}\right) + \frac{2\xi}{N}\sum_{i=l+1}^{N} \ln\left|\frac{\mathbf{x}_i-\mathbf{x}_l}{R}\right| \right\} \tag{119}$$

is the contribution from individual decondensed counterions (labeled by $l=1,\ldots,m$). Assuming that the decondensed counterions are decorrelated from other counterions as they diffuse to infinity for $\Delta\to\infty$ (i.e., using $|\mathbf{x}_i-\mathbf{x}_l|\simeq r_l$), $\mathcal{Z}_N^{(l)}$ approximately factorizes as

$$\mathcal{Z}_N^{(l)} \simeq 2\pi\int_R^D r_l\, dr_l \exp\left\{ -2\xi \ln\left(\frac{r_l}{R}\right) + \frac{2\xi}{N}\sum_{i=l+1}^{N} \ln\left(\frac{r_l}{R}\right) \right\}$$
$$= 2\pi R^2 \frac{\exp[2(1-\xi l/N)\Delta]-1}{2(1-\xi l/N)}. \tag{120}$$

In the limit $\Delta\to\infty$, $\mathcal{Z}_N^{(l)}$ diverges for

$$\xi \leqslant \frac{N}{l}, \tag{121}$$

which indicates decondensation of the lth counterion from the charged cylinder (see Sec. II D for the special case $N=1$). Repeating the above argument for various number of decondensed counterions, one finds a set of singular Manning parameters,

$$\xi_l^s \equiv \frac{N}{l} \quad \text{for } l=1,\ldots,N, \tag{122}$$

at which individual counterions decondense (condense). These singular points coincide with those obtained from our simulations based on the full partition function (114) for very large Δ (see Figs. 14–16 and Table I for numerical values).

2. Energy and heat capacity

The partition function (118) can also be written as

$$\mathcal{Z}_N = \prod_{l=1}^{N} \mathcal{Z}_N^{(l)}, \tag{123}$$

where $\mathcal{Z}_N^{(l)}$ is defined in Eq. (119). For $\Delta\gg 1$, the dominant contribution to the internal energy and the heat capacity comes from the decondensed counterions. Thus, in order to derive analytical expressions for these quantities on the leading order, we shall use Eq. (123) together with the approximate expression (120). Hence, we obtain the leading-order contribution to the free energy, $\mathcal{F}_N/(k_BT)=-\ln\mathcal{Z}_N$, as

$$\widetilde{\mathcal{F}} \equiv \frac{\mathcal{F}_N}{Nk_BT} \simeq -\frac{1}{N}\sum_{l=1}^{N} \ln\frac{e^{2(1-\xi/\xi_l^s)\Delta}-1}{2(1-\xi/\xi_l^s)}. \tag{124}$$

The rescaled internal energy $\widetilde{E}=\xi\partial\widetilde{\mathcal{F}}/\partial\xi$ and the rescaled heat capacity $\widetilde{C}=-\xi^2\partial^2\widetilde{\mathcal{F}}/\partial\xi^2$ read

$$\widetilde{E} \simeq \frac{1}{N}\sum_{l=1}^{N}\left(\frac{\xi}{\xi_l^s}\right)\left(\frac{2\Delta\exp[2(1-\xi/\xi_l^s)\Delta]}{\exp[2(1-\xi/\xi_l^s)\Delta]-1} - \frac{1}{1-\xi/\xi_l^s}\right), \tag{125}$$

$$\widetilde{C} \simeq \frac{1}{N}\sum_{l=1}^{N}\left(\frac{\xi}{\xi_l^s}\right)^2\left(\frac{1}{(1-\xi/\xi_l^s)^2} - \frac{\Delta^2}{\sinh^2[(1-\xi/\xi_l^s)\Delta]}\right) \tag{126}$$

for $\Delta\gg 1$. The above analytical expressions are shown in Figs. 15 and 16 for $\Delta=300$ and various number of particles (dashed curves), which as seen closely reproduce the behavior obtained in the simulations (symbols).

Note that as an individual counterion decondenses at ξ_l^s, the internal energy suddenly jumps, since the decondensing counterion gains a large amount of energy due to its logarithmic interaction with the central cylinder. The *regular* regions (between two successive jumps) in the energy curve are dominated by decondensed counterions and thus exhibit linear scaling with $\Delta=\ln(D/R)$. The asymptotic form of the energy curve for $\Delta\to\infty$ in these regions is obtained from Eq. (125) as

$$\lim_{\Delta\to\infty}\frac{\widetilde{E}}{\Delta} = \frac{l(l+1)}{N^2}\xi \quad \text{for} \quad \xi_{l+1}^s < \xi < \xi_l^s. \tag{127}$$

The *singular* part of the energy corresponds to a narrow region around each ξ_l^s, which (except for the uppermost singularity) is bounded between a local minimum (slightly above ξ_l^s) and a local maximum (slightly below ξ_l^s). The approximate location of these extrema are obtained using Eq. (125) as

$$\frac{\xi_l^{\min}}{\xi_l^s} \simeq 1+\frac{1}{\sqrt{\Delta(l-1)}}, \quad \frac{\xi_l^{\max}}{\xi_l^s} \simeq 1-\frac{1}{\sqrt{\Delta(l+1)}} \tag{128}$$

for large Δ. The *energy jump* $\delta\widetilde{E}_l$ upon decondensation of a counterions at $\xi=\xi_l^s$ is obtained as

$$\delta\widetilde{E}_l \equiv \widetilde{E}(\xi_l^{\max}) - \widetilde{E}(\xi_l^{\min}) \simeq \frac{2\Delta}{N}. \tag{129}$$

For $\Delta\to\infty$ but at *fixed* and *finite* N, the quantity $\widetilde{E}/\Delta$ adopts a sharp sawtoothlike form as both $\xi_l^{\min}$ and $\xi_l^{\max}$ tend to ξ_l^s producing N steplike singularities. The limiting energy jump is then given by

$$\lim_{\Delta\to\infty}\frac{\delta\widetilde{E}_l}{\Delta} = \frac{2}{N}, \tag{130}$$

which can also be obtained directly from Eq. (127).

A close examination of Eq. (125) reveals an algebraic contribution as $\sim(1-\xi_l^s/\xi)^{-1}$ to the energy in the singular region around ξ_l^s that gives rise to a diverging heat capacity for $\Delta\to\infty$. The heat capacity expression, Eq. (126), in fact exhibits N isolated peaks for large Δ. It diverges at ξ_l^s as $\widetilde{C}(\xi=\xi_l^s)\simeq\Delta^2/(3N)$ with increasing Δ to infinity and eventually, adopts N limiting algebraic singularities—i.e.,

$$\lim_{\Delta\to\infty}\widetilde{C}=\frac{1}{N}\sum_{l=1}^{N}\left(1-\frac{\xi_l^s}{\xi}\right)^{-2}. \tag{131}$$

D. Critical point and the continuum limit

The lowermost singularity at $\xi=\xi_N^s$ is associated with the decondensation of the "last" counterion from the charged cylinder. As shown above, this singularity occurs at unity ($\xi_N^s=1$) when $\Delta\to\infty$ and is thus independent of the number of counterions. It therefore gives the exact location of the 2D critical point as $\xi_c=1$ when the continuum (thermodynamic) limit $N\to\infty$ is approached. This result coincides with the mean-field prediction. [Note that in analogy with the method used in Sec. VI B, ξ_c can also be determined from the asymptotic value of the energy maximum location, Eq. (128), for $l=N$, as Δ and N increase to infinity.]

Equations (127)–(131) represent the asymptotic results when the system size increases to infinity but the number of particles, N, is finite. In the converse limiting case—i.e., when Δ is *large* and *fixed* but N increases to infinity (continuum limit)—all singularities smoothen except for the one which represents the critical point. The limiting energy curve for $N\to\infty$ may be obtained as follows. First, note that the width of the energy jump around each singularity tends to zero as indicated by Eq. (129). Second, the spacing between singular points ξ_l^s (and thus the width of regular regions for $\xi>1$) tends to zero (as $\sim 1/N$) as N increases. Therefore, the energy at a given Manning parameter ξ between two successive singularities, $\xi_{l+1}^s<\xi<\xi_l^s$, is approximately given by $\widetilde{E}\simeq\widetilde{E}(\xi=\xi_l^s)$, where the right-hand side is obtained from Eq. (125) as $\widetilde{E}(\xi=\xi_l^s)=\Delta/\xi_l^s$. This implies that

$$\lim_{N\to\infty}\widetilde{E}=\frac{\Delta}{\xi} \tag{132}$$

for $\xi\geqslant 1$ and sufficiently large Δ. For Manning parameter $\xi<1$, there are no singularities and from Eq. (125) we obtain

$$\lim_{N\to\infty}\widetilde{E}=2\xi\Delta\lim_{N\to\infty}\sum_{l=1}^{N}\frac{1}{N\xi_l^s}=\xi\Delta. \tag{133}$$

These limiting results can also be derived from Eq. (127).

The energy curve in the continuum limit therefore coincides with the universal form obtained within mean-field theory [see Eq. (61) in Sec. III D]. The heat capacity in this limit follows from Eq. (117) and exhibits a universal jump at $\xi_c=1$ in agreement with Eq. (62).

E. Condensed fraction in 2D

The preceding results enable us to calculate the limiting condensed fraction $\alpha(\xi)$ of counterions when $\Delta\to\infty$ and $N\to\infty$. For a given Manning parameter ξ and number of particles, N, the condensed fraction $\alpha_N(\xi)$ is given by the number of singularities located below ξ—i.e.,

$$\alpha_N(\xi)\equiv 1-\frac{l}{N}\quad\text{for }\xi_{l+1}^s<\xi<\xi_l^s. \tag{134}$$

This fraction is trivially zero for $\xi<\xi_c=1$ as $\Delta\to\infty$. Using Eqs. (122) and (134), we obtain the condition

$$\alpha_N(\xi)-\frac{1}{N}<1-\frac{1}{\xi}<\alpha_N(\xi), \tag{135}$$

which in the limit of infinite number of counterions yields

$$\alpha(\xi)\equiv\lim_{N\to\infty}\alpha_N(\xi)=1-\frac{1}{\xi}. \tag{136}$$

This is nothing but the mean-field or Manning condensed fraction $\alpha_M=1-1/\xi$ (Sec. VI A 2). The finite-number correction to this limiting value follows from Eq. (135) as

$$0<\alpha_N(\xi)-\alpha(\xi)<N^{-1}. \tag{137}$$

IX. CONCLUSION AND DISCUSSION

In this paper, we present the results of an extensive numerical and analytical investigation on the critical behavior of counterions at a charged cylinder in two and three spatial dimensions. Analytical results are derived using the asymptotic theories of mean field (Poisson-Boltzmann) and strong coupling. The counterion-condensation transition is controlled by the dimensionless Manning parameter (rescaled inverse temperature) $\xi=q\ell_B\tau$ and occurs at a critical threshold ξ_c, below which counterions completely unbind (decondense) to infinity, but above ξ_c, a finite fraction of counterions binds (or condenses) in the vicinity of the charged cylinder. Since the CCT criticality emerges asymptotically in the limit of infinite system size and infinitely many particles, we have employed Monte Carlo simulation of a one-dimensionally periodic cylindrical cell model in the *logarithmic radial coordinate*. This leads to a powerful (centrifugal) sampling method for extremely large lateral system sizes within reasonable equilibration times. It constitutes the key part of the present numerical investigation, since the critical and universal aspects of the CCT within the cylindrical cell model can be captured only for large *logarithmic* system size $\Delta=\ln(D/R)\gg 1$ (with D and R being the outer boundary and the charged cylinder radii, respectively).

As the main results, we have determined the precise location of the critical Manning parameter ξ_c, the scaling universality class of the CCT, and the singular behavior of the internal energy and heat capacity on a systematic level and without suppressing the inter-particle correlations. As shown both the internal energy and the heat capacity become singular at the critical point. The heat capacity, which vanishes in the decondensation phase, shows a universal discontinuity (jump) at the critical point indicating that the CCT is a second-order transition, as also suggested in a recent mean-field study [40]. In a finite system, these singularities appear

in the form of pronounced peaks; the asymptotic behavior of the peak location is used to determine the critical Manning parameter ξ_c within the simulations. On the other hand, the critical exponents associated with the CCT are obtained using a combined finite-ion-number, N, and finite-system-size, Δ, analysis of the order parameters $S_n=\langle 1/\tilde{r}^n\rangle$ where $n>0$ and $\tilde{r}=r/\mu$ is the radial distance from the cylinder axis in units of the Gouy-Chapman length μ. These order parameters represent the mean inverse localization length of counterions. For $\xi<\xi_c$ and in the limit $\Delta\to\infty$ and $N\to\infty$, S_n vanishes, but remains finite above ξ_c exhibiting the scaling relation $S_n\sim\zeta^\chi$, where $0<\zeta=1-\xi_c/\xi\ll 1$ is the reduced Manning parameter (reduced temperature). The exponent χ is determined as $\chi=2.0\pm0.4$ within our MC simulations. In a finite system, S_n does not vanish at ξ_c and displays a power-law decay with size parameters Δ and N as $S_n(\xi=\xi_c)\sim\Delta^{-\gamma}$ (when the number of particles $N\gg 1$ is fixed) and $S_n(\xi=\xi_c)\sim N^{-\nu}$ (when the lateral extension parameter $\Delta\gg 1$ is fixed), where the critical exponents are determined in our simulations as $\gamma=2.0\pm0.6$ and $\nu=2/3\pm0.1$.

The critical exponents are demonstrated to be *universal*; i.e., they are independent of the coupling strength Ξ (varied over several decades $0.1<\Xi<10^5$). They agree with the values we obtained from mean-field theory—namely, $\chi_{\mathrm{PB}}=2.0$ and $\gamma_{\mathrm{PB}}=2.0$ (the exponent ν is not defined within mean-field theory). Interestingly, the critical Manning parameter $\xi_c=1.000\pm0.002$ is also universal; it agrees with the mean-field prediction in both 3D and 2D. Therefore, in striking contrast with the typical situation in bulk critical phenomena, where deviations from mean-field theory due to fluctuations grow with decreasing dimension, the CCT criticality is found to be described by the mean-field universality class in both 3D and 2D. The mean-field theory is found to be *exact* in 2D in the whole range of Manning parameters (rescaled temperatures) when $N\to\infty$. In 3D, however, correlation effects in the condensation phase ($\xi>\xi_c$) lead to strong deviations from mean-field theory and induce a crossover to the strong-coupling theory, which exhibits a larger accumulation of counterions near the cylinder surface. This behavior has also been observed in previous numerical studies [25,42,74–76] and experiments [83]. An important result, however, is that the large-distance form of the counterion density profile remains unaffected by these correlations and thereby a *universal condensed fraction* (equal to the Manning or PB limiting value) is obtained when the inflection-point criterion is applied.

To our knowledge, a rigorous analytical derivation for the critical Manning parameter or the scaling exponents is not yet available in 3D and our simulations [28] provide the first numerical results for the universal and critical features of the CCT in the large-system-size limit. In 2D, we have shown that the simulation results can be understood using an approximate analytical theory. A more systematic approximation is developed recently in Ref. [46] that supports the present results.

The present predictions for the order parameters and thermodynamic quantities can be examined in experiments. The order parameters may be obtained from the distribution of counterions around charged polymers, which has been directly measured using anomalous scattering techniques [87]. The scaling properties of the order parameters may be investigated by changing the effective Manning parameter across the critical region using a combination of methods such as variation of the polymer linear charge density (using synthetic chains, such as ionene, or various *p*H) [17,19–21] or by variation of the dielectric constant of the medium (by mixing different solvents such as water, methanol, or ethylene glycol) [18,21]. Different regimes of the coupling parameter may be explored by, for instance, changing the charge valency of counterions; e.g., for polymer linear charge density of $\tau e\simeq 3e/\mathrm{nm}$ and radius $R\simeq 1$ nm, one can obtain a large coupling parameter $\Xi=q^3\ell_{\mathrm{B}}^2\tau/R>10$ using trivalent or tetravalent counterions such as spermidine and spermine in water and at room temperature ($\ell_{\mathrm{B}}=0.7$ nm). [Recall that the Bjerrum length $\ell_{\mathrm{B}}=e^2/(4\pi\varepsilon\varepsilon_0 k_BT)$ varies with the solvent dielectric constant and temperature.] Another quantity of interest that can be measured experimentally is the excess heat capacity of counterions, which is predicted in the present study to exhibit a universal jump at the critical Manning parameter. The heat capacity of polyelectrolyte solutions can be measured using microcalorimetry methods (see, e.g., Ref. [88] and references therein).

The two-dimensional counterion-condensation transition may be more difficult to realize experimentally. Nonetheless, mixtures of rodlike polyanions and polycations appear as good candidates for that purpose [64–66]. The central polyion could be chosen from dendronized polymers that are rigid, cylindrically shaped objects, whose radii and linear charge densities may be varied systematically. The synthesis, structural details, self-assembly, and complexation of these charged rods with other polyelectrolytes have been addressed extensively in recent years [65–67].

In this study, we have made use of an idealized (primitive) cell model [53–57] in order to bring out the main universal aspects of the CCT. Obviously, other factors that exist in realistic systems (see below) may lead to corrections to the ideal scaling relations obtained here. But the remarkable success of the cylindrical cell model in predicting various properties of polyelectrolyte solutions (such as osmotic or activity coefficients [2,41,55–57,89–91] and the counterionic density profile around polymers [83,87,92]) makes it a reliable first-step model for investigating the critical properties of the CCT as well. Due to the logarithmic convergence to the infinite-dilution limit, the limiting cell-model predictions are expected to emerge only at small polymer concentrations (as low as a few mM) [1,2,4,41,55,56,89–91]. Note that the experiments address both the salt-free (counterion-only) solutions [89,90] as well as those with additional salt concentration c_s [1,2,4,91]. In this work, we have not investigated the role of screening effects due to additional salt and coions. It is, however, known that the Debye screening length $r_s\sim c_s^{-1/2}$ plays the role of the upper bound cutoff (similar to the outer boundary D in the cell model) and that the CCT occurs strictly in the limit of zero salt concentration—i.e., when $\ln(r_s/R)\to\infty$[1,9–11,14,25,32,38,45,47]. Thus we can expect that similar asymptotic behaviors arise near $\xi_c=1$ and within a similar model as used here, when the zero-salt limit is approached. Yet it would be interesting to examine the critical salt-screening finite-size effects in a systematic fashion.

Other interesting issues for future research include investigating possible effects due to more realistic and specific factors such as the discrete charge pattern of polymers [26,27,31,39,42,75,93], chain flexibility, and finite contour length [11,12,24,26,27,31,35,36,43,94] as well as the influence of nonuniform dielectric boundaries [43,93] on the critical behavior. Note that the present results indicate that short-range effects such as electrostatic correlations do not affect the properties of the system near the critical point, because most of the counterions are decondensed and the critical behavior is predominately determined by long-range features. (The mean-field results in Refs. [42,44] similarly indicate that ion-size effects are negligible in the infinite-dilution limit.) Future studies should determine the influence of short-range specific effects in a more systematic manner.

ACKNOWLEDGMENTS

We are grateful to H. Boroudjerdi, Y. Burak, G.S. Manning, A.G. Moreira, H. Orland, R. Podgornik, and Y.Y. Suzuki for useful discussions and valuable comments. We acknowledge financial support from the DFG German-French Network.

APPENDIX A: SINGULARITIES ASSOCIATED WITH THE ONSAGER INSTABILITY

The rescaled energy $\tilde{E}=E_N/(Nk_BT)$ and the rescaled heat capacity $\tilde{C}=C_N/(Nk_B)$ associated with the Onsager instability can be calculated from Eq. (17). The results coincide with those obtained in Sec. VIII C by choosing $N=1$. In brief, the approximate location of the energy peak ξ_*^E is obtained as

$$\xi_*^E \simeq 1-\frac{1}{\sqrt{2\Delta}} \tag{A1}$$

for large Δ. This relation exhibits a different asymptotic convergency (from below) to the critical value $\xi_c=1$ as compared to the mean-field result, Eq. (83). The heat capacity peak is located above the critical point at

$$\xi_*^C \simeq 1+\frac{5}{\Delta^2}. \tag{A2}$$

In the limit $\Delta\to\infty$, the heat capacity diverges at the critical point from above and below as

$$\tilde{C}\sim\zeta^{-2}, \tag{A3}$$

where $\zeta=1-\xi_c/\xi$. The left tail of energy (for $\xi<\xi_*^E$) goes to infinity linearly with Δ as $\tilde{E}\simeq 2\xi\Delta+\xi/(\xi-1)$, but its right tail shows a power-law divergency as

$$\tilde{E}\sim\zeta^{-1}. \tag{A4}$$

Note that these behaviors are distinctly different from those obtained with many particles in the simulations and mean-field theory (Secs. VI B and III D).

APPENDIX B: RESCALED PB EQUATION

The Poisson-Boltzmann equation for mean electrostatic potential $\varphi_{\rm PB}$ in actual units reads

$$\nabla_{\mathbf{x}}^2\varphi_{\rm PB}=\frac{\sigma(\mathbf{x})e}{\varepsilon\varepsilon_0}-\frac{qe\rho_{\rm PB}(\mathbf{x})}{\varepsilon\varepsilon_0}, \tag{B1}$$

where the density profile of counterions is given by

$$\rho_{\rm PB}(\mathbf{x})=\rho_0\Omega(\mathbf{x})e^{-qe\varphi_{\rm PB}(\mathbf{x})/k_BT}, \tag{B2}$$

with ρ_0 being a normalization prefactor and $\Omega(\mathbf{x})$ specifying the volume accessible to counterions [Eq. (20)]. The rescaled PB equation (18) is recovered using Eqs. (B1) and (B2) and the dimensionless quantities $\tilde{\mathbf{x}}=\mathbf{x}/\mu$, $\tilde{\sigma}(\tilde{\mathbf{x}})=\mu\sigma(\mathbf{x})/\sigma_s$, $\tilde{\rho}_{\rm PB}(\tilde{\mathbf{x}})=\rho_{\rm PB}(\mathbf{x})/(2\pi\ell_{\rm B}\sigma_s^2)$, $\psi_{\rm PB}=qe\varphi_{\rm PB}/(k_BT)$, where $\mu=R/\xi=1/(2\pi q\ell_{\rm B}\sigma_s)$ is the Gouy-Chapman length [Eq. (6)]. The prefactor ρ_0 is related to $\tilde{\kappa}$ in Eq. (18) through $\tilde{\kappa}=\kappa\mu$ where $\kappa^2=4\pi q^2\ell_{\rm B}\rho_0$. One can show that the actual density profile (B2) is also mapped to the rescaled profile (23).

Normalization of the density (to the total number of counterions) in actual units reads $\int d\mathbf{x}\,\rho_{\rm PB}(\mathbf{x})=N$, and in rescaled units, we have $\int d\tilde{\mathbf{x}}\,\tilde{\rho}_{\rm PB}(\tilde{\mathbf{x}})=2\pi\Xi N$, which is equivalent to Eq. (21) in the text, when Eqs. (11) and (23) are used.

APPENDIX C: ASYMPTOTIC RESULTS WITHIN THE PB THEORY

1. Limiting behavior of β for large Δ

A general discussion of the global behavior of β has been given by Fuoss *et al.* [54] using Eq. (26). Here, we first review some of their results as quoted in the text and then derive the finite-size-scaling relations for β near the PB critical point ($\xi_c^{\rm PB}=1$) as used in Sec. III C.

A. Small Manning parameter $\xi<\Lambda_*$

The integration constant β vanishes at $\xi=\Lambda_*=\Delta/(1+\Delta)$ and tends to unity, $\beta\to 1^-$, for small $\xi\to 0^+$, as can be checked easily from Eq. (26) (we arbitrarily choose $\beta\geqslant 0$). Further inspection shows that in this regime, $\beta\to(1-\xi)^-$ when $\Delta\to\infty$ [54]. Hence for $\Delta\gg 1$, one can propose the following form:

$$\beta^2\simeq(1-\xi)^2(1-x), \tag{C1}$$

where x is a small function of ξ and Δ. To determine x, we may rearrange the first equation in Eq. (26) as

$$\beta\Delta=\frac{1}{2}\ln\frac{1-\beta}{1+\beta}-\frac{1}{2}\ln\frac{(\xi-1)+\beta}{(\xi-1)-\beta} \tag{C2}$$

and use this together with Eq. (C1) to obtain

$$x\simeq\frac{4\xi}{2-\xi}e^{-2(1-\xi)\Delta}. \tag{C3}$$

This reproduces Eq. (31) in the text.

B. Large Manning parameter $\xi>\Lambda_*$

One can easily show that β, Eq. (26), is a monotonically increasing function of ξ for finite Δ; it vanishes at $\xi=\Lambda_*$ and tends to a finite upper bound $\beta_\infty=\pi/\Delta$ when $\xi\to\infty$ [54]. Thus in the limit $\Delta\to\infty$, β vanishes for the whole range of

Manning parameters $\xi > \Lambda_* \to 1^-$. This result was frequently used in the text [see, e.g., Eqs. (41) and (42)].

C. Finite-size scaling for β close to $\xi_c^{\rm PB}$

Of particular importance in our analysis is the behavior of β close to $\xi_c^{\rm PB}=1$. (Since always $\Lambda_* \leqslant 1$, we restrict the discussion only to the regime $\xi \geqslant \Lambda_*$.) Analysis of Eq. (26) shows that for sufficiently large Δ, we have $\beta \simeq \pi/(2\Delta)$ right at the critical point $\xi_c^{\rm PB}=1$. We may then perform a Taylor expansion around $\xi_c^{\rm PB}$ to obtain the approximate form of β for small $\zeta = 1 - \xi_c^{\rm PB}/\xi$ as

$$\beta(\zeta,\Delta) = \frac{\pi}{2\Delta} + \frac{2}{\pi}\zeta - \frac{8\Delta}{\pi^3}\zeta^2 + O(\zeta^3), \tag{C4}$$

which remains valid for $\zeta\Delta < \pi^2/4$. This relation clearly indicates a scale-invariant form for β when $\Delta \gg 1$. Comparing this with Eq. (50), we find the approximate form of the scaling function $\mathcal{B}(u)$ as

$$\mathcal{B}(u) \simeq \frac{\pi}{2} + \frac{2}{\pi}u - \frac{8}{\pi^3}u^2, \tag{C5}$$

where $u = \zeta\Delta < \pi^2/4$. In particular, we have $\mathcal{B}(u) \to \pi/2$ as $u \to 0$.

The asymptotic behavior of $\mathcal{B}(u)$ for $u \to \infty$ (or, equivalently, $\Delta \to \infty$ for finite ζ) can be obtained using a different series expansion, since in this limit β becomes singular at $\xi_c^{\rm PB}=1$ and the above expansion breaks down. This is because β is always singular (with an infinite first derivative) at Λ_* which tends to the critical Manning parameter when $\Delta \to \infty$. We thus perform a singular expansion around $\xi=\Lambda_*$, which yields $\beta \simeq \sqrt{3\zeta/\Delta}$. Hence, the asymptotic form of the scaling function is given by

$$\mathcal{B}(u) \simeq \sqrt{3u}, \quad u \to \infty. \tag{C6}$$

2. PB cumulative density profile

The PB cumulative density of counterions, $n_{\rm PB}(y)$, is defined via Eq. (73). It can easily be shown that $n_{\rm PB}(y)$ is a monotonically increasing function of $y=\ln(r/R)$—i.e., $dn_{\rm PB}/dy > 0$. It is therefore bounded by its boundary values $n_{\rm PB}(0)=0$ and $n_{\rm PB}(\Delta)=N$ (Fig. 3).

For $\xi > \Lambda_*$, $n_{\rm PB}(y)$ has an inflection point the location of which, $y_*=\ln(r_*/R)$, follows from the equation $d^2 n_{\rm PB}/dy^2 = 0$ as $y_* = \tan^{-1}[(\xi-1)/\beta]/\beta$. It is easy to check (using the results in Appendix C 1) that $y_* \simeq \Delta/2$ for large ξ and that $y_* \to 0$ for $\xi \to 1$. For $\xi < \Lambda_*$, on the other hand, the cumulative density $n_{\rm PB}(y)$ vanishes for $y < \Delta$ when $\Delta \to \infty$, as can be checked by inserting the approximate expression (C1) for β into Eq. (73).

We note that the main quantities of interest within the PB theory can be expressed solely in terms of the cumulative density profile. This includes the PB potential field $\psi_{\rm PB}$ and the order parameter $S_n^{\rm PB}$. Using the definitions of these quantities (Sec. III), we obtain the following relations (which are valid for all ξ):

$$\psi_{\rm PB}(y) = 2\xi\left(y - \frac{1}{N}\int_0^y n_{\rm PB}(y')dy' \right), \tag{C7}$$

$$S_n^{\rm PB} = \frac{1}{\xi^n}\int_0^\Delta dy\, e^{-ny}\left(\frac{1}{N}\frac{dn_{\rm PB}}{dy} \right). \tag{C8}$$

3. Asymptotic behavior of S_n within PB theory

A. Small Manning parameter $\xi < \Lambda_*$

For $\xi < \Lambda_*$, the order parameter $S_n^{\rm PB}$ vanishes as $\Delta \to \infty$, indicating complete decondensation of counterions. To demonstrate this result, we use Eq. (C8), which, for $\Delta \gg 1$, can be written as

$$\xi^n S_n^{\rm PB} = \frac{n}{N}\int_0^\Delta dy\, e^{-ny} n_{\rm PB}(y) + O(e^{-n\Delta}). \tag{C9}$$

Since the cumulative density is bounded by the number of counterions, N, and tends to zero at any finite y for $\xi < \Lambda_*$ (Appendix C 2), we obtain $S_n^{\rm PB} \to 0$ in this regime when $\Delta \to \infty$.

B. Large Manning parameter $\xi > \Lambda_*$

Consider the exact mean-field expression for $S_n^{\rm PB}$, Eq. (40). The integrand in Eq. (40) is the product of an exponentially decaying factor with an inverse-squared sine function, which has a series of divergencies at $y_m=(m\pi-\epsilon)/\beta$ for integer m and $\epsilon \equiv \cot^{-1}[(\xi-1)/\beta]$. For $\Delta \to \infty$, we have $\beta \to 0$ when $\xi > \Lambda_*$ (Appendix C 1), implying $\epsilon \to 0$. In this limit, ϵ may be expanded as

$$\epsilon \simeq \frac{\beta}{\xi-1} - \frac{\beta^3}{3(\xi-1)^3} + O(\beta^5). \tag{C10}$$

The location of singularities, y_m, tends to infinity as Δ increases except for $m=0$ for which we have $y_0 = -\epsilon/\beta \to -1/(\xi-1)$ using Eq. (C10). The quantity $S_n^{\rm PB}$ in Eq. (40) is therefore dominated by the lower boundary of the integral (around $y=0$) due to the exponentially decaying integrand. To derive the asymptotic form of $S_n^{\rm PB}$ for large Δ, one can expand the integrand either around $y=0$ or around the singular point y_0. Both procedures lead to the same scaling relation (42) for $S_n^{\rm PB}$ in the strict limit of $\Delta \to \infty$ when ξ is *close* to the critical value $\xi_c^{\rm PB}=1$. But as ξ becomes larger ($\xi > 1$), only the second procedure leads to the correct result, because the singularity at $y_0 \sim -1/(\xi-1)$ approaches zero, rendering the expansion around $y=0$ a poor approximation.

By expanding the integrand around $y=0$ (up to the first order in y), we obtain from Eq. (40) that

$$S_n^{\rm PB} \simeq \frac{\beta^2}{\xi^{n+1}\sin^2\epsilon}\int_0^\Delta dy\, e^{-(n+2\xi-2)y} \simeq \frac{\beta^2 + (\xi-1)^2}{\xi^{n+1}(n+2\xi-2)}. \tag{C11}$$

This relation reproduces Eq. (41) in the text, which, as explained above, is valid for ξ close to $\xi_c^{\rm PB}=1$.

For larger values of ξ, we expand the integrand in Eq. (40) around $y_0=-\epsilon/\beta$, which yields

$$S_n^{\mathrm{PB}} \simeq \frac{\beta/\epsilon}{\xi^{n+1}}\left[1-\frac{n\epsilon}{\beta}e^{n\epsilon/\beta}\Gamma\left(0,\frac{n\epsilon}{\beta}\right)\right], \tag{C12}$$

where $\Gamma(a,b)$ is the incomplete gamma function. This relation provides a reasonably good approximation for S_n^{PB} at large Δ and in the whole range $\xi>1$. In particular, when the limit $\Delta\to\infty$ is taken, it yields the correct analytical result as expressed in Eq. (C18) below.

4. PB solution in an unbounded system ($\Delta=\infty$)

In the present study, we have assumed that the counterion-cylinder system is bounded laterally, ensuring that the normalization of density profile $\tilde{\rho}_{\mathrm{PB}}(\tilde{r})$ to the total number of counterions, N, is fulfilled even in the limit $\Delta\to\infty$. In a strictly unbounded system (with $\Delta=\infty$), this normalization condition is not preserved, because a finite fraction of counterions can escape to infinity. In this case, the PB equation (18) can be solved by relaxing the normalization condition (21) and assuming the boundary conditions at the cylinder surface as $\psi_{\mathrm{PB}}^{\infty}(\tilde{R})=0$ and $\tilde{R}[d\psi_{\mathrm{PB}}^{\infty}(\tilde{r}=\tilde{R})/d\tilde{r}]=2\xi$. One thus finds [70]

$$\psi_{\mathrm{PB}}^{\infty}(\tilde{r})=\begin{cases}2\xi\ln\dfrac{\tilde{r}}{\tilde{R}}, & \xi\leqslant 1,\\ 2\ln\dfrac{\tilde{r}}{\tilde{R}}+2\ln\left[1+(\xi-1)\ln\dfrac{\tilde{r}}{\tilde{R}}\right], & \xi\geqslant 1,\end{cases} \tag{C13}$$

and that $\tilde{\kappa}^2/2=\tilde{\rho}_{\mathrm{PB}}^{\infty}(\tilde{R})=0$ for $\xi\leqslant 1$ and $\tilde{\kappa}^2/2=(\xi-1)^2/\xi^2$ otherwise. Hence using Eq. (23), the density profile in an unbounded system (for $\tilde{R}\leqslant\tilde{r}\leqslant\tilde{D}$) reads

$$\tilde{\rho}_{\mathrm{PB}}^{\infty}(\tilde{r})=\begin{cases}0, & \xi\leqslant 1,\\ \dfrac{(\xi-1)^2}{\xi^2}\left[\dfrac{\tilde{r}}{\tilde{R}}\right]^{-2}\left[1+(\xi-1)\ln\dfrac{\tilde{r}}{\tilde{R}}\right]^{-2}, & \xi\geqslant 1,\end{cases} \tag{C14}$$

which coincides with the asymptotic expressions (32) and (34). But now $\tilde{\rho}_{\mathrm{PB}}^{\infty}(\tilde{r})$ is normalized only to the condensed fraction α_{M} [Eq. (72)]—i.e.,

$$\int_{\tilde{R}}^{\infty} d\tilde{r}\,\tilde{r}\,\tilde{\rho}_{\mathrm{PB}}^{\infty}(\tilde{r})=\alpha_{\mathrm{M}}\xi=\begin{cases}0, & \xi\leqslant 1,\\ \xi-1, & \xi\geqslant 1\end{cases} \tag{C15}$$

[compare with Eq. (29) and note the order in which the integration and the infinite-system-size limit are taken]. The order parameter in an unbounded system, $S_n^{\mathrm{PB},\infty}$, may be calculated using $\tilde{\rho}_{\mathrm{PB}}^{\infty}$. For $\xi\geqslant\xi_c^{\mathrm{PB}}=1$, we obtain

$$S_n^{\mathrm{PB},\infty}=\frac{1}{\xi^n}\left[1-\frac{n}{\xi-1}e^{n/(\xi-1)}\Gamma\left(0,\frac{n}{\xi-1}\right)\right]. \tag{C16}$$

Near the critical point ($0<\zeta=1-\xi_c^{\mathrm{PB}}/\xi\ll 1$), we have

$$S_n^{\mathrm{PB},\infty}(\zeta)\simeq\frac{\zeta}{n}, \tag{C17}$$

which exhibits a different exponent as compared with the quantity $S_n^{\mathrm{PB}}(\zeta,\Delta\to\infty)$ in Eq. (42). This is again due to the difference in the normalization factor, which enters in S_n through Eq. (38). In general, however, the limiting ($\Delta\to\infty$) result for the order parameter S_n^{PB}, Eq. (40), may be obtained for *arbitrary* ξ by multiplying $S_n^{\mathrm{PB},\infty}$ in Eq. (C16) with the condensed fraction α_{M}—i.e.,

$$\lim_{\Delta\to\infty} S_n^{\mathrm{PB}}=\alpha_{\mathrm{M}}S_n^{\mathrm{PB},\infty}. \tag{C18}$$

APPENDIX D: HAMILTONIAN OF A PERIODIC CYLINDRICAL CELL MODEL (3D)

As stated in Sec. V B, the periodic boundary conditions used in the simulations in 3D lead to summation of the Coulomb interaction [$v_{3\mathrm{D}}(\mathbf{x})=1/|\mathbf{x}|$] over an infinite number of periodic images. For an *electroneutral* system, the resultant summation series are convergent and can be mapped to fast-converging series that can be handled easily in the simulations [78,79]. In what follows, we derive the convergent expressions for the Hamiltonian (3).

The main (cylindrical) simulation box (of height L and containing N counterions) is replicated infinitely many times in the z direction, generating a series of $M\to\infty$ image boxes labeled by the index $m=-M/2,\ldots,-1,0,1,\ldots,+M/2$ (with $m=0$ being the main box). The Hamiltonian (3) consists of three parts $\mathcal{H}_N=\mathcal{H}_{\mathrm{ci}}+\mathcal{H}_{\mathrm{int}}+\mathcal{H}_{\mathrm{self}}$—namely, the counterion-counterion interaction $\mathcal{H}_{\mathrm{ci}}$, the counterion-cylinder interaction $\mathcal{H}_{\mathrm{int}}$, and the cylinder self-energy $\mathcal{H}_{\mathrm{self}}$, which will be analyzed separately. (Here we use actual units and in the end, transform the results to the rescaled form.)

1. $\mathcal{H}_{\mathrm{int}}$ and $\mathcal{H}_{\mathrm{self}}$ terms

The counterion-cylinder interaction part per simulation box reads $\mathcal{H}_{\mathrm{int}}/(Mk_BT)=\sum_{\alpha=1}^{N}u(r_\alpha)$, where, using $\sigma(\mathbf{x})=\sigma_s\delta(r-R)$, we have

$$u(r_\alpha)=-q\ell_{\mathrm{B}}\int v_{3\mathrm{D}}(\mathbf{x}-\mathbf{x}_\alpha)\sigma(\mathbf{x})\,d\mathbf{x}=2\xi\ln\left(\frac{r_\alpha}{R}\right)+c_0, \tag{D1}$$

with α running only over the counterions within the main box. The constant term is given by

$$c_0=-q\ell_{\mathrm{B}}\int v_{3\mathrm{D}}(\mathbf{x}-\mathbf{x}_0)\sigma(\mathbf{x})\,d\mathbf{x}, \tag{D2}$$

where $\mathbf{x}_0$ belongs to the cylinder (equipotential) surface. c_0 may be written in terms of the cylinder self-energy,

$$\frac{\mathcal{H}_{\mathrm{self}}}{Mk_BT}=\frac{\ell_{\mathrm{B}}}{2}\int\sigma(\mathbf{x})v_{3\mathrm{D}}(\mathbf{x}-\mathbf{x}')\sigma(\mathbf{x}')\,d\mathbf{x}\,d\mathbf{x}'. \tag{D3}$$

Using the electroneutrality condition $\tau L=qN$ (per box), one can show that $\mathcal{H}_{\mathrm{self}}/(Mk_BT)=-Nc_0/2$. Hence

$$\frac{1}{Mk_BT}(\mathcal{H}_{\mathrm{int}}+\mathcal{H}_{\mathrm{self}})=2\xi\sum_{\alpha=1}^{N}\ln\left(\frac{r_\alpha}{R}\right)+C_0, \tag{D4}$$

where $C_0=-\mathcal{H}_{\mathrm{self}}/(Mk_BT)$ is a constant, which diverges logarithmically with M. This can be seen from the asymptotic

behavior of the self-energy for large M (or large ML/R)—i.e.,

$$\frac{\mathcal{H}_{\rm self}/(k_BT)}{\tau^2\ell_{\rm B}ML} = \int_0^{2\pi}\frac{d\theta\,d\theta'}{4\pi^2}\int_{-ML/2}^{ML/2}\frac{dz\,dz'/(2ML)}{\sqrt{(z-z')^2+4R^2\sin^2[(\theta-\theta')/2]}} \simeq a_0+\ln\left(\frac{ML}{R}\right)+O\left(\frac{R}{ML}\right), \tag{D5}$$

where $a_0\simeq\ln 2-1$. This logarithmic divergency is canceled by a similar divergent term coming from the interaction between counterions as we show now.

2. $\mathcal{H}_{\rm ci}$ term and the Lekner-Sperb formula

The contribution from counterionic interactions (per simulation box and for large M) can be written as

$$\frac{\mathcal{H}_{\rm ci}}{Mk_BT}=\frac{q^2\ell_{\rm B}}{2M}\sum_{i\neq j}v_{\rm 3D}(\mathbf{x}_i-\mathbf{x}_j) =\frac{q^2\ell_{\rm B}}{2L}\left[\sum_{\alpha\neq\beta}S_M\left(\frac{\mathbf{x}_\alpha-\mathbf{x}_\beta}{L}\right)+NS_M^0\right], \tag{D6}$$

where i and j run over *all* counterions (including periodic images), while α and β ($\alpha,\beta=1,\ldots,N$) run over counterions in the main simulation box. We have defined $S_M^0=2\Sigma_{m=1}^{M/2}m^{-1}$ and

$$S_M\left(\frac{\mathbf{x}_\alpha-\mathbf{x}_\beta}{L}\right)=\sum_{m=-M/2}^{M/2}[\rho_{\alpha\beta}^2+(\zeta_{\alpha\beta}+m)^2]^{-1/2}, \tag{D7}$$

where $\rho_{\alpha\beta}=[(x_\alpha-x_\beta)^2+(y_\alpha-y_\beta)^2]^{1/2}/L$ and $\zeta_{\alpha\beta}=(z_\alpha-z_\beta)/L$. Note that, in particular, S_M^0 represents the interaction between a counterion and its periodic images, which are lined up in the z direction. This series diverges and may be written as $S_M^0=2\ln(M/2)+2\mathbf{C}_e$ for $M\to\infty$, where $\mathbf{C}_e=0.577\,215\ldots$ is the Euler's constant. In this limit, S_M is also divergent, but it may be split into a convergent and a divergent part as

$$S_M=S_M^0+S_{\rm LS}(\rho_{\alpha\beta},\zeta_{\alpha\beta})+2(\ln 2-\mathbf{C}_e), \tag{D8}$$

in which the convergent series $S_{\rm LS}(\rho_{\alpha\beta},\zeta_{\alpha\beta})$ can be expressed in terms of the special functions [78,79].

Now inserting the above results for S_M and S_M^0 into Eq. (D6), we have, for $M\to\infty$,

$$\frac{\mathcal{H}_{\rm ci}}{Mk_BT}=\frac{q^2\ell_{\rm B}}{2L}\sum_{\alpha\neq\beta}S_{\rm LS}(\rho_{\alpha\beta},\zeta_{\alpha\beta})+\xi(\mathbf{C}_e-\ln 2)+\xi N\ln M, \tag{D9}$$

with a logarithmic divergent term (last term) from the one-dimensional periodicity of the system. It immediately follows that the divergencies in Eqs. (D4) and (D9) cancel each other when the electroneutrality condition is imposed. Thus we have the well-defined expression

$$\frac{\mathcal{H}_N}{Mk_BT}=2\xi\sum_{\alpha=1}^{N}\ln\left(\frac{r_\alpha}{R}\right)+\frac{q^2\ell_{\rm B}}{2L}\sum_{\alpha\neq\beta}S_{\rm LS}(\rho_{\alpha\beta},\zeta_{\alpha\beta})+\xi Nh_0, \tag{D10}$$

where $h_0=1+\ln(R/2L)+(\mathbf{C}_e-\ln 2)/N$; equivalently,

$$\frac{\mathcal{H}_N}{Mk_BT}=2\xi\sum_{\alpha=1}^{N}\ln\left(\frac{\tilde r_\alpha}{\tilde R}\right)+\frac{\Xi}{2\tilde L}\sum_{\alpha\neq\beta}S_{\rm LS}(\tilde\rho_{\alpha\beta},\tilde\zeta_{\alpha\beta})+\xi Nh_0 \tag{D11}$$

in rescaled units, where $h_0=1+\ln(\xi^2/2\Xi N)+(\mathbf{C}_e-\ln 2)/N$. The above expression is used to calculate the internal energy and the heat capacity in our simulations (Sec. VI). The term $S_{\rm LS}(\tilde\rho_{\alpha\beta},\tilde\zeta_{\alpha\beta})$ may be determined from Eq. (D8) using some mathematical identities as shown by Lekner [78] and Sperb [79]. It may be written in the form of two formally *identical* series expansions

$$S_{\rm LS}=\begin{cases}-2\ln\tilde\rho_{\alpha\beta}+4\sum_{m=1}^{\infty}K_0(2\pi m\tilde\rho_{\alpha\beta})\cos(2\pi m\tilde\zeta_{\alpha\beta}) & \text{(series I)}\\ \sum_{m=1}^{\infty}\binom{-1/2}{m}(\tilde\rho_{\alpha\beta})^{2m}[Z(2m+1,1+\tilde\zeta_{\alpha\beta})+Z(2m+1,1-\tilde\zeta_{\alpha\beta})]+(\tilde\rho_{\alpha\beta}^2+\tilde\zeta_{\alpha\beta}^2)^{-1/2}-\Psi(1+\tilde\zeta_{\alpha\beta})-\Psi(1-\tilde\zeta_{\alpha\beta})-c_* & \text{(series II)}.\end{cases} \tag{D12}$$

In the above relations, $K_0(x)$ is the modified Bessel function of the second kind, $Z(n,x)=\Sigma_{k=0}^{\infty}1/(k+x)^n$ is the Hurwitz zeta function, $\Psi(x)$ is the digamma function, and $c_*=2\ln 2\simeq 1.386\,294\ldots$.

The series in Eq. (D12) can be evaluated numerically up to the desired accuracy. Note that the first series (Lekner scheme) involves the Bessel function $K_0(x)$, which decays exponentially for large x [as $\sim\exp(-x)/\sqrt{x}$] but diverges logarithmically for small x. It is therefore rapidly converging when the rescaled radial distance between two given particles, $\tilde\rho_{\alpha\beta}$, is sufficiently large. We use the following recipe to truncate series I: For $\tilde\rho_{\alpha\beta}>3$, we

truncate after the third term, for $1/3 \leqslant \tilde{\rho}_{\alpha\beta} \leqslant 3$, we include $2+[3/\tilde{\rho}_{\alpha\beta}]$ terms in the sum (where $[x]$ refers to the integer part of x), and for $1/4 \leqslant \tilde{\rho}_{\alpha\beta} < 1/3$, we sum at least 12 terms. This recipe ensures a *relative* truncation error of about $|e_r| \sim 10^{-10}$. For small radial separation $\tilde{\rho}_{\alpha\beta} < 1/4$ between two particles, series I becomes inefficient and slow. We thus employ the second series expression (Sperb scheme). This series is rapidly converging for small $\tilde{\rho}_{\alpha\beta}$ provided that $\tilde{\zeta}_{\alpha\beta}$, which enters in the argument of the Hurwitz zeta function, is sufficiently small—namely, for $|\tilde{\zeta}_{\alpha\beta}| \leqslant 1/2$ [79] (note that in general we have $|\tilde{\zeta}_{\alpha\beta}| \leqslant 1$). In fact, due to the periodicity of the system, the energy expression (D6) remains invariant under the transformations $\tilde{\zeta}_{\alpha\beta} \to 1 - \tilde{\zeta}_{\alpha\beta}$ and $\tilde{\zeta}_{\alpha\beta} \to -\tilde{\zeta}_{\alpha\beta}$, and thus $\tilde{\zeta}_{\alpha\beta}$ can always be restricted to the range $|\tilde{\zeta}_{\alpha\beta}| \leqslant 1/2$. In this case, we use up to eight terms in series II. The relative truncation error $|e_r|$ varies for different $\tilde{\zeta}_{\alpha\beta}$; e.g., for $\tilde{\zeta}_{\alpha\beta} \simeq 0.4$ and $\tilde{\rho}_{\alpha\beta} \simeq 0.25$, one has $|e_r| \sim 10^{-7}$. The error substantially decreases for smaller $\tilde{\zeta}_{\alpha\beta}$. The above truncation recipes yield very accurate estimates for the interaction energies within the statistical error bars of the simulations.

[1] G. S. Manning, J. Chem. Phys. **51**, 924 (1969); **51**, 3249 (1969).
[2] F. Oosawa, *Polyelectrolytes* (Marcel Dekker, New York, 1971).
[3] N. Imai and T. Ohnishi, J. Chem. Phys. **30**, 1115 (1959); T. Ohnishi, N. Imai, and F. Oosawa, J. Phys. Soc. Jpn. **15**, 896 (1960).
[4] G. S. Manning, Biophys. Chem. **7**, 95 (1977).
[5] G. S. Manning, J. Phys. Chem. **79**, 262 (1975); **85**, 1506 (1981).
[6] G. S. Manning, Q. Rev. Biophys. **11**, 179 (1978).
[7] G. S. Manning, Ber. Bunsenges. Phys. Chem. **100**, 909 (1996).
[8] G. S. Manning, Physica A **231**, 236 (1996).
[9] A. D. MacGillivray, J. Chem. Phys. **56**, 80 (1972); **56**, 83 (1972); **57**, 4071 (1972); **57**, 4075 (1972).
[10] G. V. Ramanathan, J. Chem. Phys. **78**, 3223 (1983).
[11] G. V. Ramanathan and C. P. Woodbury, J. Chem. Phys. **77**, 4133 (1982); **82**, 1482 (1985).
[12] C. P. Woodbury and G. V. Ramanathan, Macromolecules **15**, 82 (1982).
[13] B. H. Zimm and M. Le Bret, J. Biomol. Struct. Dyn. **1**, 461 (1983); M. Le Bret and B. H. Zimm, Bull. Pol. Acad. Sci., Chem. **32**, 287 (1984).
[14] J. S. McCaskill and E. D. Fackerell, J. Chem. Soc., Faraday Trans. 2 **84**, 161 (1988).
[15] A. Ikegami, J. Polym. Sci., Part A: Gen. Pap. **2**, 907 (1964).
[16] R. Zana *et al.*, J. Chim. Phys. Phys.-Chim. Biol. **68**, 1258 (1971).
[17] M. Kowblansky and P. Zema, Macromolecules **14**, 166 (1981); **14**, 1448 (1981).
[18] J. W. Klein and B. R. Ware, J. Chem. Phys. **80**, 1334 (1984).
[19] P. Ander and M. Kardan, Macromolecules **17**, 2431 (1984).
[20] L. M. Penafiel and T. A. Litovitz, J. Chem. Phys. **96**, 3033 (1992); **97**, 559 (1992).
[21] A. Popov and D. A. Hoagland, J. Polym. Sci., Part B: Polym. Phys. **42**, 3616 (2004).
[22] J. X. Tang *et al.*, Biochemistry **36**, 12600 (1997); G. C. L. Wong, A. Lin, J. X. Tang, Y. Li, P. A. Janmey, and C. R. Safinya, Phys. Rev. Lett. **91**, 018103 (2003).
[23] V. Bloomfield, Biopolymers **31**, 1471 (1991); Curr. Opin. Struct. Biol. **6**, 334 (1996).
[24] R. G. Winkler, M. Gold, and P. Reineker, Phys. Rev. Lett. **80**, 3731 (1998).
[25] M. Deserno, C. Holm, and S. May, Macromolecules **33**, 199 (2000).
[26] S. Liu and M. Muthukumar, J. Chem. Phys. **116**, 9975 (2002); S. Liu, K. Ghosh, and M. Muthukumar, J. Chem. Phys. **119**, 1813 (2003).
[27] Q. Liao, A. V. Dobrynin, and M. Rubinstein, Macromolecules **36**, 3399 (2003).
[28] A. Naji and R. R. Netz, Phys. Rev. Lett. **95**, 185703 (2005).
[29] M. Fixman, J. Chem. Phys. **70**, 4995 (1979).
[30] D. Stigter, J. Phys. Chem. **82**, 1603 (1978); Biophys. J. **69**, 380 (1995).
[31] P. González-Mozuelos and M. Olvera de la Cruz, J. Chem. Phys. **103**, 3145 (1995).
[32] C. A. Tracy and H. Widom, Physica A **244**, 402 (1997).
[33] Y. Levin and M. C. Barbosa, J. Phys. II **7**, 37 (1997).
[34] P. S. Kuhn, Y. Levin, and M. C. Barbosa, Macromolecules **31**, 8347 (1998).
[35] H. Schiessel and P. Pincus, Macromolecules **31**, 7953 (1998).
[36] R. M. Nyquist, B.-Y. Ha, and A. J. Liu, Macromolecules **32**, 3481 (1999).
[37] J. Ray and G. S. Manning, Macromolecules **32**, 4588 (1999).
[38] H. Qian and J. A. Schellman, J. Phys. Chem. B **104**, 11528 (2000).
[39] G. S. Manning, Macromolecules **34**, 4650 (2001).
[40] A. Deshkovski, S. Obukhov, and M. Rubinstein, Phys. Rev. Lett. **86**, 2341 (2001).
[41] P. L. Hansen, R. Podgornik, and V. A. Parsegian, Phys. Rev. E **64**, 021907 (2001).
[42] M. L. Henle, C. D. Santangelo, D. M. Patel, and P. A. Pincus, Europhys. Lett. **66**, 284 (2004).
[43] M. Muthukumar, J. Chem. Phys. **120**, 9343 (2004).
[44] I. Borukhov, J. Polym. Sci., Part B: Polym. Phys. **42**, 3598 (2004).
[45] B. O'Shaughnessy and Q. Yang, Phys. Rev. Lett. **94**, 048302 (2005).
[46] Y. Burak and H. Orland, Phys. Rev. E **73**, 010501(R) (2006).
[47] E. Trizac and G. Téllez, Phys. Rev. Lett. **96**, 038302 (2006).
[48] A. L. Kholodenko and A. L. Beyerlein, Phys. Rev. Lett. **74**, 4679 (1995).
[49] Y. Levin, Physica A **257**, 408 (1998).
[50] Y. Y. Suzuki, J. Phys.: Condens. Matter **16**, 2119 (2004).
[51] R. L. Cleland, Macromolecules **24**, 4386 (1991).
[52] J. Cardy, *Scaling and Renormalization in Statistical Physics* (Cambridge University Press, Cambridge, England, 1996).

[53] T. Alfrey, P. W. Berg, and H. Morawetz, J. Polym. Sci. **7**, 543 (1951).
[54] R. M. Fuoss, A. Katchalsky, and S. Lifson, Proc. Natl. Acad. Sci. U.S.A. **37**, 579 (1951).
[55] S. Lifson and A. Katchalsky, J. Polym. Sci. **13**, 43 (1954).
[56] A. Katchalsky, Pure Appl. Chem. **26**, 327 (1971).
[57] R. A. Marcus, J. Chem. Phys. **23**, 1057 (1955).
[58] A. Yu. Grosberg, T. T. Nguyen, and B. I. Shklovskii, Rev. Mod. Phys. **74**, 329 (2002); Y. Levin, Rep. Prog. Phys. **65**, 1577 (2002).
[59] R. R. Netz, Eur. Phys. J. E **5**, 557 (2001).
[60] A. G. Moreira and R. R. Netz, Eur. Phys. J. E **8**, 33 (2002); Europhys. Lett. **52**, 705 (2000).
[61] A. Naji and R. R. Netz, Eur. Phys. J. E **13**, 43 (2004); A. Naji, A. Arnold, C. Holm, and R. R. Netz, Europhys. Lett. **67**, 130 (2004).
[62] A. Naji, S. Jungblut, A. G. Moreira, and R. R. Netz, Physica A **352**, 131 (2005).
[63] H. Boroudjerdi, Y.-W. Kim, A. Naji, R. R. Netz, X. Schlagberger, and A. Serr, Phys. Rep. **416**, 129 (2005).
[64] J. DeRouchey, R. R. Netz, and J. O. Rädler, Eur. Phys. J. E **16**, 17 (2005).
[65] I. Gössl *et al.*, J. Am. Chem. Soc. **124**, 6860 (2002).
[66] N. Severin, J. P. Rabe, and D. G. Kurth, J. Am. Chem. Soc. **126**, 3696 (2004).
[67] W. Stocker *et al.*, J. Am. Chem. Soc. **120**, 7691 (1998).
[68] The Onsager divergency may equivalently occur when the lower bound of the integral (cylinder radius) tends to zero—i.e., $R \to 0$ [1]—since only the ratio D/R is relevant.
[69] Y. Burak, D. Andelman, and H. Orland, Phys. Rev. E **70**, 016102 (2004).
[70] R. R. Netz and J.-F. Joanny, Macromolecules **31**, 5123 (1998).
[71] Note that the density moments for $n < 0$ are divergent since, for finite ξ, a finite fraction of counterions is always decondensed.
[72] M. Kardar and R. Golestanian, Rev. Mod. Phys. **71**, 1233 (1999).
[73] A. Naji, R. R. Netz, and C. Seidel, Eur. Phys. J. E **12**, 223 (2003).
[74] D. Bratko and V. Vlachy, Chem. Phys. Lett. **90**, 434 (1982).
[75] M. Le Bret and B. H. Zimm, Biopolymers **23**, 271 (1984).
[76] C. S. Murthy, R. J. Bacquet, and P. J. Rossky, J. Phys. Chem. **89**, 701 (1985).
[77] N. Metropolis *et al.*, J. Chem. Phys. **21**, 1087 (1953).
[78] J. Lekner, Physica A **176**, 485 (1991).
[79] R. Sperb, Mol. Simul. **20**, 179 (1998).
[80] A. Arnold and C. Holm, Comput. Phys. Commun. **148**, 327 (2002).
[81] H. Flyvberg and H. G. Petersen, J. Chem. Phys. **91**, 461 (1989).
[82] R. Bacquet and P. J. Rossky, J. Phys. Chem. **88**, 2660 (1984).
[83] S. S. Zakharova *et al.*, J. Chem. Phys. **111**, 10706 (1999).
[84] K. Binder and D. W. Heermann, *Monte Carlo Simulation in Statistical Physics: An Introduction* (Springer-Verlag, Berlin, 1997).
[85] A. M. Ferrenberg and D. P. Landau, Phys. Rev. B **44**, 5081 (1991).
[86] M. E. Fisher and M. N. Barber, Phys. Rev. Lett. **28**, 1516 (1972).
[87] R. Das, T. T. Mills, L. W. Kwok, G. S. Maskel, I. S. Millett, S. Doniach, K. D. Finkelstein, D. Herschlag, and L. Pollack, Phys. Rev. Lett. **90**, 188103 (2003).
[88] Z. Kiraly and G. H. Findenegg, Langmuir **21**, 5047 (2005).
[89] M. Deserno *et al.*, Eur. Phys. J. E **5**, 97 (2001).
[90] H. E. Auer and Z. Alexandrowicz, Biopolymers **8**, 1 (1969).
[91] E. Raspaud, M. da Conceiçao, and F. Livolant, Phys. Rev. Lett. **84**, 2533 (2000).
[92] F. Muller *et al.*, Eur. Phys. J. E **6**, 109 (2001).
[93] B. Jayaram *et al.*, Macromolecules **23**, 3156 (1990).
[94] M. J. Stevens and K. Kremer, J. Chem. Phys. **103**, 1669 (1995).